Cell Reports

Article

A planar polarized MYO6-DOCK7-RAC1 axis promotes tissue fluidification in mammary epithelia

Graphical abstract

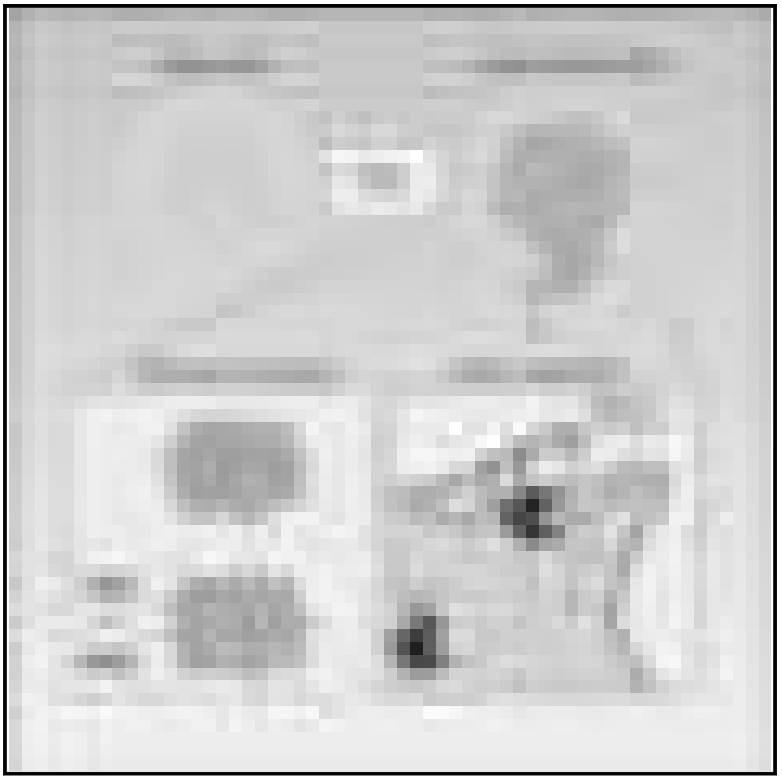

Authors

Luca Menin, Janine Weber, Stefano Villa, ..., Fabio Giavazzi, Giorgio Scita, Simona Polo

Correspondence

giorgio.scita@ifom.eu (G.S.), simona.polo@ifom.eu (S.P.)

In brief

Menin et al. reveal that the collective motion of jammed epithelia depends on a MYO6-DOCK7-RAC1 axis operating specifically in follower cells. Activation of this pathway promotes the orientation and persistence of cryptic lamellipodia, enabling long-range coordination of movements of epithelial cells during tissue fluidification, wound repair, and invasive outgrowth.

Highlights

- Collective motion of jammed epithelia requires myosin VI
- MYO6-DOCK7 axis is critical to restrict activity of RAC1 in a planar polarized fashion
- MYO6-DOCK7-RAC1 axis ensures long-range coordination of movements in follower cells
- Myosin VI short expression is elevated in infiltrating breast cancer cells

Menin et al., 2023, Cell Reports *42*, 113001
August 29, 2023
https://doi.org/10.1016/j.celrep.2023.113001

CellPress

Cell Reports

CellPress
OPEN ACCESS

Article

A planar polarized MYO6-DOCK7-RAC1 axis promotes tissue fluidification in mammary epithelia

Luca Menin,[1,8] Janine Weber,[1,9] Stefano Villa,[2,10] Emanuele Martini,[1] Elena Maspero,[1] Carlos A. Niño,[1] Valeria Cancila,[3] Alessandro Poli,[1] Paolo Maiuri,[4] Andrea Palamidessi,[1] Emanuela Frittoli,[1] Fabrizio Bianchi,[5] Claudio Tripodo,[1,3] Kylie J. Walters,[6] Fabio Giavazzi,[2] Giorgio Scita,[1,7,*] and Simona Polo[1,7,11,*]

[1]IFOM ETS, The AIRC Institute of Molecular Oncology, Milan, Italy
[2]Dipartimento di Biotecnologie Mediche e Medicina Traslazionale, Università degli Studi di Milano, Segrate, Italy
[3]Human Pathology Section, Department of Health Sciences, University of Palermo School of Medicine, Palermo, Italy
[4]Department of Molecular Medicine and Medical Biotechnology, University of Naples Federico II, Naples, Italy
[5]Unit of Cancer Biomarkers, Fondazione IRCCS Casa Sollievo della Sofferenza, San Giovanni Rotondo, Italy
[6]Protein Processing Section, Center for Structural Biology, Center for Cancer Research, National Cancer Institute, National Institutes of Health, Frederick, MD 21702, USA
[7]Dipartimento di Oncologia ed Emato-oncologia, Università degli Studi di Milano, Milan, Italy
[8]Present address: Università degli Studi di Milano, Milan, Italy
[9]Present address: Human Technopole, Milan, Italy
[10]Present address: Max Planck Institute for Dynamics and Self-Organization, Göttingen, Germany
[11]Lead contact
*Correspondence: giorgio.scita@ifom.eu (G.S.), simona.polo@ifom.eu (S.P.)
https://doi.org/10.1016/j.celrep.2023.113001

SUMMARY

Tissue fluidification and collective motility are pivotal in regulating embryonic morphogenesis, wound healing, and tumor metastasis. These processes frequently require that each cell constituent of a tissue coordinates its migration activity and directed motion through the oriented extension of lamellipodium cell protrusions, promoted by RAC1 activity. While the upstream RAC1 regulators in individual migratory cells or leader cells during invasion or wound healing are well characterized, how RAC1 is controlled in follower cells remains unknown. Here, we identify a MYO6-DOCK7 axis essential for spatially restricting RAC1 activity in a planar polarized fashion in model tissue monolayers. The MYO6-DOCK7 axis specifically controls the extension of cryptic lamellipodia required to drive tissue fluidification and cooperative-mode motion in otherwise solid and static carcinoma cell collectives.

INTRODUCTION

Collective motility and tissue fluidification are emerging as key regulators in physiological tissue remodeling during development, wound repair, and regeneration and in pathological conditions, first and foremost during carcinoma dissemination.[1–5] During these processes, individual cells composing a given tissue coordinate their motion with that of their neighbor cells by keeping tight cell-cell contacts to migrate or invade.[6]

A remarkable form of collective dynamics occurs during the early development of epithelial and glandular tissues, which are characterized by individual cells that constantly rearrange their motion, as in a fluid. This fluid-like property endows tissues with a large degree of plasticity that is instrumental in the initial phases of tissue specification and morphogenesis. As density rises because of proliferation and tissues mature and differentiate, the motion of each cell is constrained by the crowding of its neighbors, forcing cells to move in groups in a highly coordinated and cooperative fashion.[7,8] At a critical density, motility ceases, and tissues rigidify to undergo a fluid-to-solid phase transition, a process recently referred to as a jamming transition.[9] This tissue-level phase transition has been proposed to be critical for development of the elastic properties and barrier function of epithelial tissues and might also act as an intrinsic homeostatic mechanical barrier to development and expansion of structurally altered, hyperdynamic oncogenic clones. Conversely, a certain degree of fluidity is needed for a tissue to repair a wound, proliferate, or locally disseminate, such as during carcinoma progression.[1,4]

Tissue fluidification and collective motility are ruled by biochemical and physical interactions cells establish with each other and their environment.[2,10] How cells and tissues regulate this process and control these parameters has only begun to be investigated. To drive and propel directed cell migration, cells need to dynamically reorganize their actin cytoskeleton and generate actively pushing lamellipodial cell protrusions.[11] When embedded in a fully confluent monolayer or a developing epithelial tissue, cell protrusions can no longer extend into free space but are forced to either push adjacent neighboring cells or slip underneath them and are commonly referred to as cryptic lamellipodia.[12] Coordinated and directed extension of cryptic lamellipodia along a common direction drives groups of cells

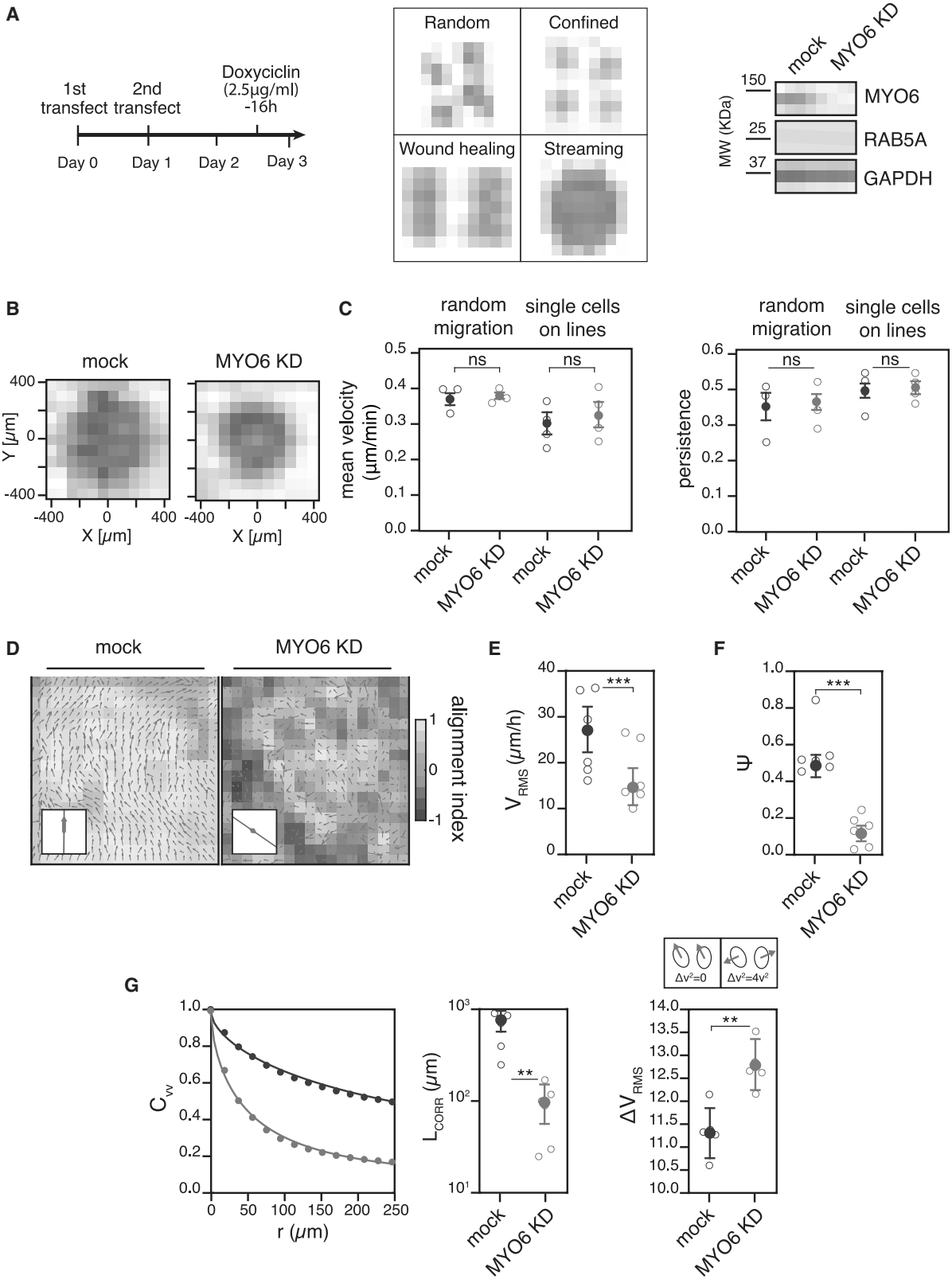

(legend on next page)

to move either as a solid rotating flock, such as in the case of the follicular epithelial cells in *Drosophila melanogaster*,[13] or as supracellular streams that fluidize the whole tissue, as during compression- or endocytosis-driven unjamming of human bronchial epithelial tissue and model mammary epithelial cells.[14,15]

We have shown previously that elevated levels of RAB5A, a master regulator of early endosomes, is sufficient to re-awaken the motility of otherwise kinetically arrested epithelial monolayers, promoting millimeter-scale flocking-fluid motility through large-scale coordinated migration and local cell rearrangements.[14,16–18] At the molecular level, RAB5A impinges on junction topology, turnover, and tension, fostering extension of oriented and coordinated cryptic lamellipodia.[14,17] The leading edges of cryptic lamellipodia, much like those of individual crawling cells, are generated by localized and spatially restricted actin polymerization triggered by numerous actin regulators and coordinated by the small GTPase RAC1.[14,19] However, the molecular machinery driving cryptic lamellipodium protrusion is likely to be distinct or enriched with specific components with respect to more canonical lamellipodia of cells moving individually or into free space. Indeed, a distinct cell identity with a leader-to-follower topological organization is emerging as critical in driving directed collective motion, such as in the case of Indian-file-moving cells,[20] protruding multicellular fingers extending into the free space during wound closure in model epithelia,[21] or cell-cohort-invading stromal tissues during carcinoma dissemination.[4,22,23]

Among the proteins that regulate cell migration and membrane protrusion, myosin VI is an unconventional actin-based motor protein that moves toward the minus end of actin filaments.[24–26] Myosin VI was originally characterized in *Drosophila melanogaster*, where it participates in collective migration of border cells during ovary development.[27,28] The pro-migratory function of myosin VI has also been confirmed in tumors, where elevated levels of this protein are frequent and correlate with the aggressive behavior in ovarian, breast, and prostate cancer.[26,28–31] In epithelial carcinoma, deregulated alternative splicing results in preferential or exclusive expression of the short isoform of myosin VI, to which a cancerous malignancy becomes addicted for migration.[31] Despite the increasing interest in the potential oncogenic role of myosin VI in cell migration, little is known about its mechanism of action and potential impact on cancer collective migration capacity.

Here, we employ oncogenic monolayer models in which RAB5A expression can be tuned in an inducible fashion to promote flocking-fluid motility and test the impact of myosin VI. We uncover a myosin VI-DOCK7 axis as critical for spatially restricting the activity of RAC1 in a planar polarized fashion. Myosin VI is specifically required in follower cells to promote formation of cryptic lamellipodia that drive tissue fluidification by triggering highly coordinated and cooperative-mode motion in otherwise solid and static carcinoma cell collectives.

RESULTS

Myosin VI is critical for coherent motion of jammed epithelia

Myosin VI is required for cancer cell migration through an ill-defined molecular mechanism.[25,31] We examined the role of myosin VI during individual and collective cell migration; namely, during random and confined migration of single cells or in wound healing and tissue fluidification via flocking stream in epithelial monolayers (Figure 1A). To directly compare the results, we exploited the oncogenically transformed MCF10.DCIS.com cell line, in which collective streaming of cells in densely packed and confluent monolayers can be induced by modulation of RAB5A expression[14] (hereafter referred to as ductal in situ carcinoma [DCIS]-RAB5A). This cell line uniquely expresses the short isoform of myosin VI (Figure S1A) and, thus, represents the ideal model system to identify specific roles of this isoform.

Silencing of myosin VI with specific small interfering RNA (siRNA) oligos had no impact on the mean velocity or persistence of motility of individual cells in random or confined migration assays (Figures 1B and 1C; Videos S1 and S2). Conversely, in wound healing experiments, myosin VI depletion caused impairment of collective migration, consistent with previous findings.[31] The defective collective motion is the result of a reduction in the global velocity of wound closure (Figure S1B; Video S3), likely because of impairment of cell directionality (Figure S1C). A second siRNA myosin VI oligo showed similar depletion efficiency and almost identical results (Figures S1D and S1E).

We then analyzed the reawakening of collective migratory properties during unjamming of otherwise solid and static epithelial monolayers. Time-lapse image sequences of control and knockdown (KD) cells were analyzed by particle image velocimetry

Figure 1. Myosin VI is required for coherent motion of jammed epithelia

(A) Experimental pipeline used for all kinetics experiments using DCIS-RAB5A and derivative cell lines. Right: representative immunoblot (IB) analysis of the indicated lysates (day 3).

(B) Representative example of single-cell trajectories obtained from random migration assays with the indicated cell lines.

(C) Quantification of single cell motion assays with the indicated cell lines. n = 75 (25 single cells/experiment/genotype for three independent experiments). Empty circle, mean of the single experiment. Error bars, ±SD. not significant (ns) > 0.999 by Student's t test.

(D) Representative snapshots of the velocity field obtained by PIV analysis (red arrows), taken at 8 h after the beginning of the experiment. The color map represents the alignment with respect to the mean instantaneous velocity, quantified by the alignment index $a(x) = \boldsymbol{v}(x)\cdot\boldsymbol{v_0}/|\boldsymbol{v}(x)\cdot\boldsymbol{v_0}|$, which is equal to $1(-1)$ when the local velocity is parallel (antiparallel) to the mean direction of migration. Red arrows in each inset represent the mean velocity v_0 (average over the entire field of view).

(E) Root-mean-square velocity V_{RMS} parameter obtained from the PIV analysis of six independent experiments. Empty circle, mean of each experiment calculated from at least five videos/condition. Error bars, ±SD. ***p < 0.001 by Student's t test.

(F) Orientational order parameter ψ obtained from the PIV analysis described in (E). Error bars, ±SD. ***p < 0.001 by Student's t test.

(G) Left: velocity correlation functions $C_{vv}(r)$ obtained from PIV analysis (symbols) and best-fitting curves with a stretched exponential model (continuous lines). Center: correlation length L_{corr} obtained from the fitting procedure, the corresponding average stretching exponent β being 0.69 ± 0.07 and 0.76 ± 0.05 for mock and MYO6 KD, respectively. Error bars, ±SD. **p < 0.01 by Student's t test. Right: mean square relative velocity Δv_{RMS} of pairs of neighboring cells obtained from nuclear tracking.

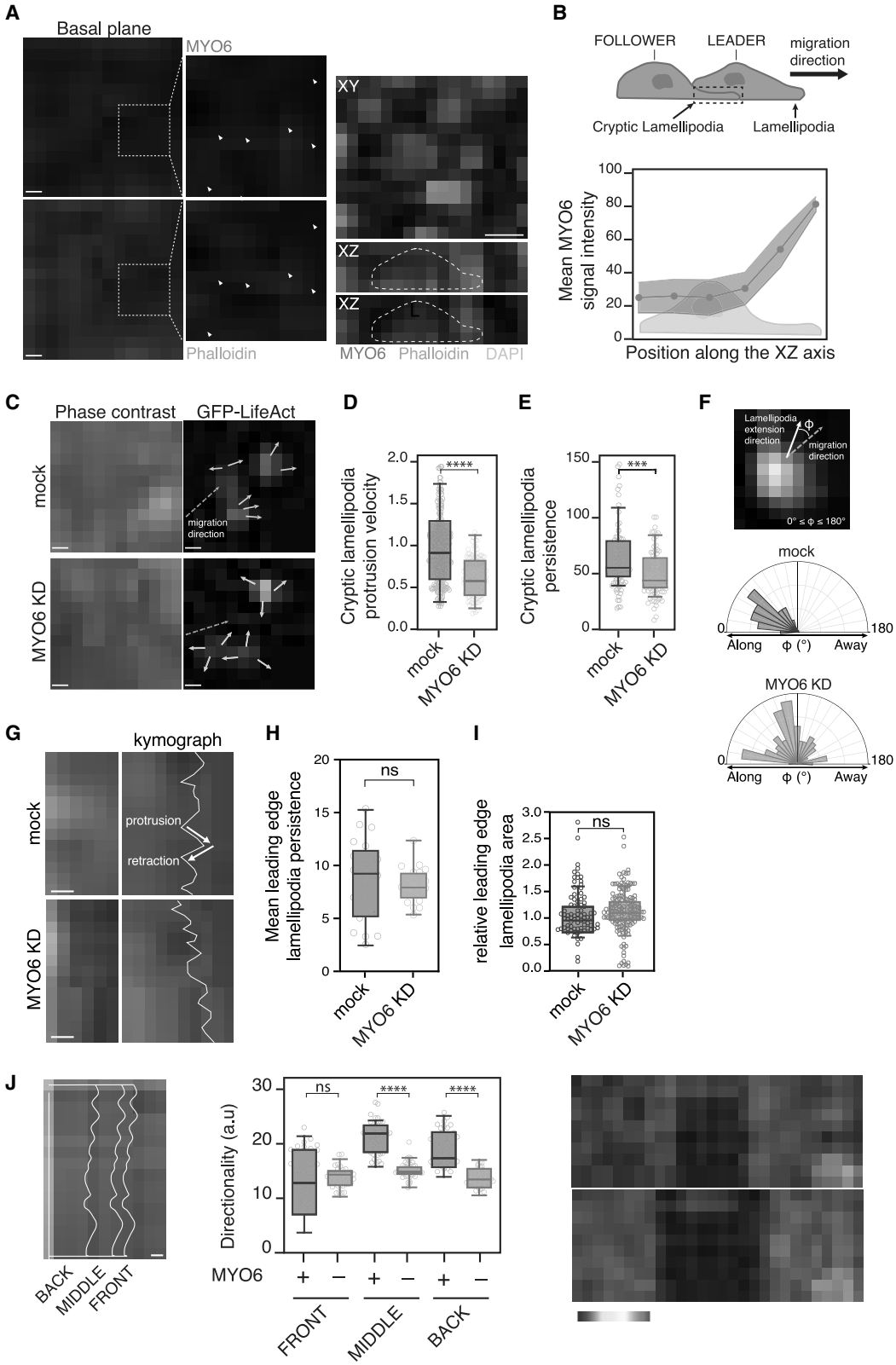

(legend on next page)

(PIV) to determine the local prevalent direction of motion and obtain time-resolved, coarse-grained velocity fields.[14] As shown in Figure 1D and Videos S4 and S5, myosin VI depletion strongly impacts collective migration by reducing the overall cellular motility, quantified by the root-mean-square velocity v_{RMS} (Figure 1E) and, even more strikingly, by severely impairing long-range cell-cell coordination. The degree of mutual alignment of cellular velocities is captured by the polar order parameter ψ, which can vary in the range of $[0,1]$, with $\psi = 1$ corresponding to a perfectly uniform velocity field and $\psi \simeq 0$ to a randomly oriented velocity field (see STAR Methods for details). While we measure $\psi \simeq 0.5$ for the control monolayer, clearly indicating the presence of directed collective migration, we observed a 4- to 5-fold decrease in ψ for the myosin VI KD condition (Figure 1F). We confirmed the lack of long-range coordination in KD monolayers by calculating the velocity correlation functions $C_{vv}(r)$ and the corresponding correlation lengths L_{corr} (Figure 1G). L_{corr}, which roughly corresponds to the characteristic linear size of a "pack" of coherently migrating cells, displays a striking 20-fold reduction in KD cells. Intriguingly, besides reducing large-scale coordination, myosin VI depletion also enhances small-scale velocity fluctuations, as can be seen by considering the mean squared relative velocity $\sqrt{(<\Delta v_{RMS}>)^2}$ of neighboring cell pairs, which displays a significant increase in KD monolayers (Figure 1G). Of note, all of these effects are not due to a cell division defect because similar numbers of cells were present in fully confluent mock and myosin VI-depleted monolayers (Figure S1F), and this collective locomotion is unperturbed by replication inhibition.[14]

Altogether, these results showed that the critical role of myosin VI in controlling multicellular streaming-like motility is an emergent property of confluent monolayers.

Myosin VI coordinates cryptic lamellipodium dynamics in follower cells

Myosin VI has been reported to be localized at adherens junctions and to interact with the cytoplasmic tail of E-cadherin.[32–34] In DCIS-RAB5 cells, myosin VI displays a diffuse cytoplasmic pattern in isolated, sparsely seeded cells but rapidly accumulates at desmosomes when a cluster of two or more cells is established (Figure S2A). In confluent monolayers, myosin VI was also present at the basal level, where it accumulated in actin-rich protrusions, called cryptic lamellipodia, which extend underneath the neighboring cells and display a planar polarized distribution[12,35] (Figures 2A and 2B). Importantly, by monitoring the dynamics of cells expressing EGFP-LifeAct interspersed with non-fluorescent cells, we found that myosin VI depletion did not impair formation of cryptic lamellipodia (Figure 2C; Video S6) but severely reduced their velocity (Figure 2D) and persistence (Figure 2E).

One striking feature of flocking-fluid locomotion in DCIS-RAB5A cells is their long-range, persistent, and ballistic motility. This trait is driven by formation of highly coordinated cryptic lamellipodia oriented in the direction of motion. Myosin VI depletion strongly impaired the alignment of these protrusions along the motility direction of supracellular motility streams (Figure 2F). Notably, myosin VI depletion specifically impaired cryptic lamellipodia in cell monolayers because its depletion did not alter the protrusion and persistence of lamellipodia generated in single cells (Figures S2B and S2C).

Cryptic lamellipodia are typically observed in follower cells during direct cell motility.[12] The streaming motility in monolayers, however, does not allow discernment of leader-to-follower topological cell organization. Thus, we analyzed myosin VI activity

Figure 2. Myosin VI coordinates cryptic lamellipodium dynamics in follower cells

(A) Basal plane of a fully confluent DCIS-RAB5A monolayer. Immunofluorescence (IF) analysis was performed as indicated. Arrows in the magnifications indicate the accumulation of myosin VI and phalloidin signals at the cryptic lamellipodia. Scale bars, 10 μm. Right panel: example of z stack projection of the same cells. Scale bars, 5 μm.

(B) Top: schematic of cryptic lamellipodium structure. Bottom: mean fluorescence signal of myosin VI across single cells from z stack acquisition images. n = 60 (4 independent experiments). Error bars, ±SD.

(C) Representative phase-contrast and fluorescence images of the streaming assay of mock or MYO6 KD monolayers where GFP-LifeAct-expressing cells were interspersed (1:10 ratio). Green arrow, direction of the migrating cell sheet. Scale bars, 15 μm.

(D) Quantification of cryptic lamellipodium protrusion velocity from the streaming assay described in (C). Results in the graph are expressed relative to GFP-LifeAct-expressing mock average value. The central mark indicates the median, and the bottom and top edges of the box indicate the 25th and 75th percentiles, respectively. An empty circle represents the mean lamellipodium protrusion velocity of a single cell. n = 145 (4 independent experiments). ****$p < 0.0001$ by Student's t test.

(E) Quantification of cryptic lamellipodium persistence from the streaming assay described in (C). Data are plotted as the number of frames in which the lamellipodium is detectable. An empty circle represents the persistence of single lamellipodia. $n \geq 74$ (4 independent experiments). ***$p < 0.001$ by Student's t test.

(F) Top: representative image of the angle Φ between the direction of the cryptic lamellipodia (white arrow) and the direction of the migrating cell sheet (green arrow). Bottom plots: quantification of the orientation angle Φ for the indicated cell lines. $n \geq 140$ (4 independent experiments).

(G) Representative phase-contrast images of leading-edge lamellipodia and their relative kymograph from scratched mock or MYO6 KD cell monolayers. Scale bars, 3 μm. Arrows in the kymograph highlight one protrusion and retraction event.

(H) Quantification of leading-edge lamellipodium persistence (expressed in minutes) obtained by kymograph analysis as in (G). An empty circle represents the persistence of single leading-edge lamellipodia. n = 20 (3 independent experiments). ns > 0.999 by Student's t test.

(I) Quantification of leading-edge lamellipodium mean area obtained by neural network[36] using phase-contrast images as in (G). Results in the graph are expressed relative to mock average value. An empty circle represents the area occupied by leading edge lamellipodia. $n \geq 80$ (4 independent experiments). ns > 0.999 by Student's t test.

(J) Single-cell tracking of the wound healing assay performed on H2B-mCherry-expressing mock or MYO6 KD cells. Left: representative phase-contrast images of the wound healing assay. White lines define the area to which cells are assigned based on their distance from the wound edge. Scale bars, 50 μm. Center, quantification of the directionality of the cells belonging to the different area expressed as the inverse of the directional change rate parameter obtained with TrackMate. An empty circle represents the mean directionality of the tracks for each time-lapse video. $n \geq 30$ (3 independent experiments). Error bars, ±SEM. ns > 0.999, ****$p < 0.0001$ by ANOVA. Right: visual representation of the tracking data quantified. Each nucleus is colored coded according to the direction persistence (from blue [high directionality] to red [low directionality]). One representative dataset is shown. Top: mock; bottom: MYO6 KD.

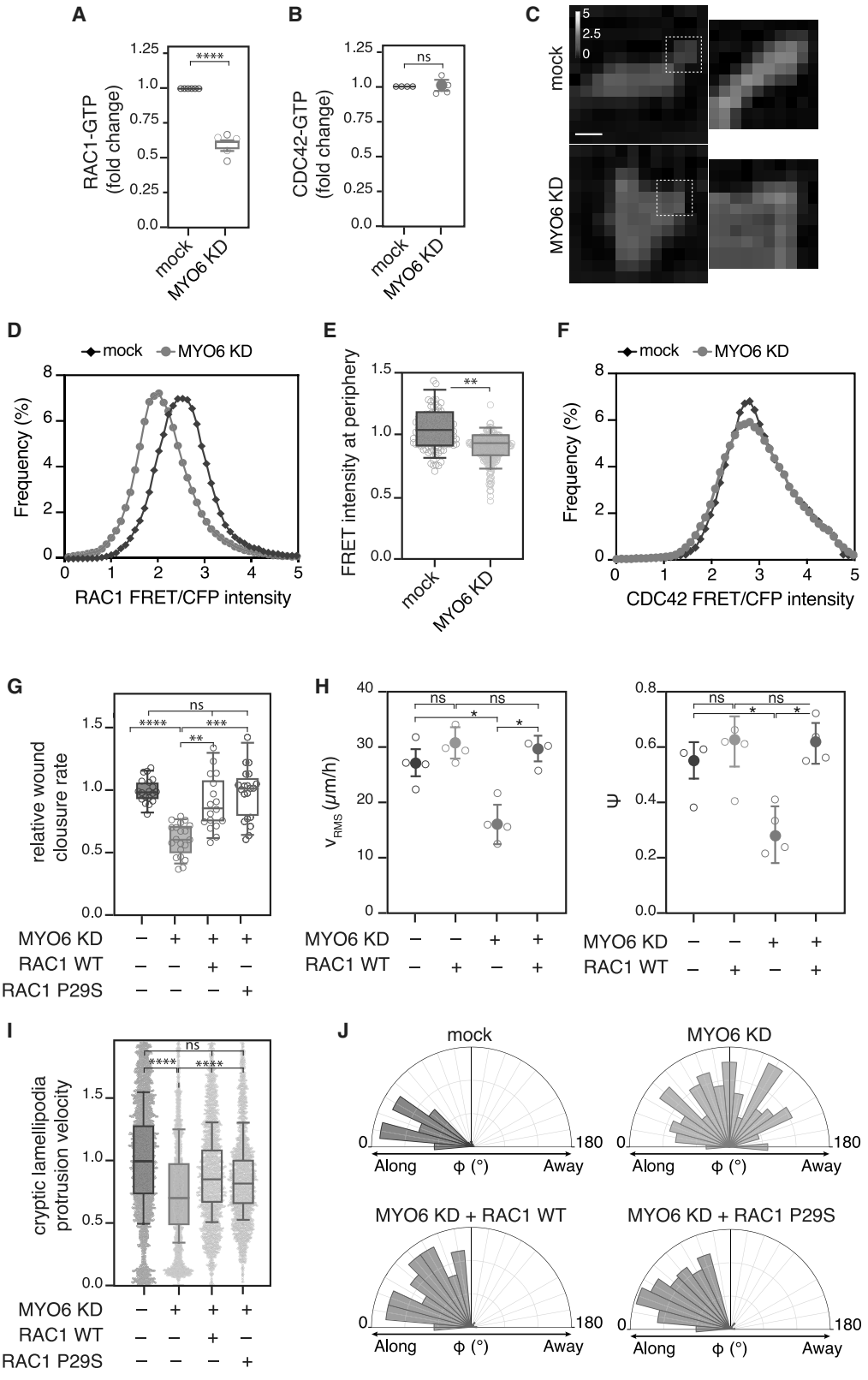

(legend on next page)

using a wound healing assay where the migratory phenotype caused by its depletion is evident (Figures S1B and S1C). For each cell, we measured its absolute speed and axial component in the direction of the wound by tracking its H2B-mCherry-labeled nucleus. Consistent with the specific role of myosin VI in the followers, silencing of the protein did not alter lamellipodium extension and persistence in leader cells at the wound front, as quantified by kymograph (Figures 2G and 2H) and neuronal network analyses[36] of the dynamics at the leading edges (Figure 2I). We also employed single-cell tracking analysis to evaluate the movement of cells located away from the wound edge. Strikingly, we found a significant reduction in cell directionality specifically in follower cells that were a few rows away from the wound edge (Figure 2J).

Collectively, these findings indicate that myosin VI specifically controls the coordinated persistence and dynamics of cryptic lamellipodia in follower cells, a prerequisite for collective movement.

Myosin VI regulates RAC1 GTPase activation at cryptic lamellipodia

A critical molecular determinant of cryptic lamellipodia is the small GTPases RAC1, whose activity is essential to trigger localized branched actin polymerization at the leading edge of migratory cells. We found that the total amount of active RAC1 was significantly reduced in myosin VI-depleted lysates from confluent cell monolayers (Figures 3A and S3A). Importantly, loss of myosin VI does not alter the level of active CDC42 (Figures 3B and S3B) or of RAC1 when lysates are prepared from isolated cells grown under sparse conditions (Figure S3C), reinforcing the notion of a specific function of myosin VI in controlling RAC1 activity in streaming, fluidized monolayers.

Next, we generated a stable DCIS-RAB5A cell line expressing a second-generation RAC1-fluorescence resonance energy transfer (FRET) biosensor.[37] Cells expressing the RAC1-FRET sensor were mosaically seeded in a confluent monolayer composed of non-fluorescent cells to enable measurement of RAC1 activation with high spatial resolution. In control cells, analysis of multiple protrusions revealed an increase in FRET activity in proximity to the cell periphery (arbitrarily estimated at a distance of 1.5 μm from the plasma membrane), consistent with the established role of RAC1 activity in cryptic lamellipodia[38,39] (Figures 3C–3E). Strikingly, depletion of myosin VI significantly reduced the relative FRET signal of RAC1 activity in protrusions (Figures 3C–3E). Importantly, absence of myosin VI did not alter activation of CDC42, measured using a specific FRET biosensor[40] (Figure 3F). These results indicate that myosin VI is essential for optimal activation of RAC1 in cryptic lamellipodia that drive coordinated, long-range streaming motility.[35]

Finally, we tested whether constitutive activation of RAC1 was sufficient to rescue the phenotypes induced by myosin VI depletion using different orthogonal approaches. First, we found that addition of the cholinergic agonist and RAC1 activator carbachol[41,42] partially rescued the wound closure defect observed upon myosin VI depletion (Figure S3D). Next, we expressed wild-type (WT) RAC1) or its fast-cycling RAC1-P29S variant[43] in EGFP-LifeAct-expressing cells after silencing of myosin VI. WT RAC1 and RAC1-P29S were sufficient to rescue the wound closure defect (Figure 3G; Video S7) as well as the streaming defect observed in myosin VI-depleted cells upon RAB5A-induced unjamming. Indeed, ectopic expression of RAC1 in the cell monolayer was sufficient to rescue the loss of cell coordination measured by spatial velocity correlation lengths and root-mean-square velocity (Figure 3H; Video S8). Finally, we tested the dynamics of cryptic lamellipodia in the flocking, confluent monolayers. Expression of WT RAC1 or RAC1-P29S effectively restored the defective cryptic lamellipodium velocity (Figure 3I) and directional orientation (Figure 3J) caused by myosin VI depletion.

Altogether, these results demonstrate that myosin VI regulates localized activation of RAC1 specifically at cryptic lamellipodium protrusions to promote coordinated and collective cell migration and tissue fluidification.

Myosin VI controls RAC1 activation in cryptic lamellipodia by recruiting DOCK7

To gain insight into the molecular mechanisms underlying myosin VI regulation of RAC1 activity, we took advantage of the myosin VI

Figure 3. Myosin VI regulates RAC1 GTPase activation at cryptic lamellipodia

(A) GST-CRIB assay quantification from mock or MYO6 KD monolayers. Data are reported as fold change with respect to RAC1-GTP level in the corresponding mock sample for each experiment. n = 5 independent experiments. Reported values are mean ± SD. ****p < 0.0001 by Student's t test.

(B) As in (A) but for CDC42-GTP. Reported values are mean ± SD. ns > 0.999 by Student's t test.

(C) Representative images of RAC1-FRET biosensor-expressing mock or MYO6 KD cells. Scale bars, 10 μm. White lines define the area used for quantification of the FRET intensity signal at the cell periphery (<1.5 μm from the edge). The intensity, represented by a color scale, is shown. Right: magnification.

(D) Representative distribution of the normalized RAC1-FRET intensity signal at the cell periphery of a mock or MYO6 KD cell.

(E) Quantification of the FRET intensity signal at the cell periphery of mock or MYO6 KD cells. Results are expressed relative to mock average value. n ≥ 117 (4 independent experiments). **p < 0.01 by Student's t test.

(F) Representative distribution of the normalized CDC42-FRET intensity signal at the cell periphery of a mock or MYO6 KD cell.

(G) Wound healing assay results for the indicated cell lines. The average wound closure speed relative to the mock condition is plotted in the graph. The empty circle represents the mean wound closure velocity quantified for each video. n = 20 (4 independent experiments). ns > 0.999, **p < 0.01, ***p < 0.001, ****p < 0.0001 by ANOVA.

(H) PIV analysis of the streaming assay performed as in Figures 1E and 1F for the indicated cell lines. Left: root-mean-square velocity, V_{RMS}. Right: orientational order parameter, ψ. Empty circle, mean of the single experiment calculated from at least five videos/condition (four independent experiments). Error bars ±SD. ns > 0.999, *p < 0.05 by ANOVA.

(I) Quantification of cryptic lamellipodium protrusion velocity performed as in Figure 2D for the indicated cell lines. Results in the graph are expressed relative to GFP-LifeAct-expressing mock average value. An empty circle represents the mean lamellipodium protrusion velocity of a single cell. n = 144 (3 independent experiments). ns > 0.999, ****p < 0.0001 by ANOVA.

(J) Quantification of the orientation angle Φ performed as in Figure 2F. n = 132 for mock and MYO6 KD cells, n = 250 for MYO6 KD cells expressing wild-type (WT) RAC1 and RAC1-P29S (3 independent experiments).

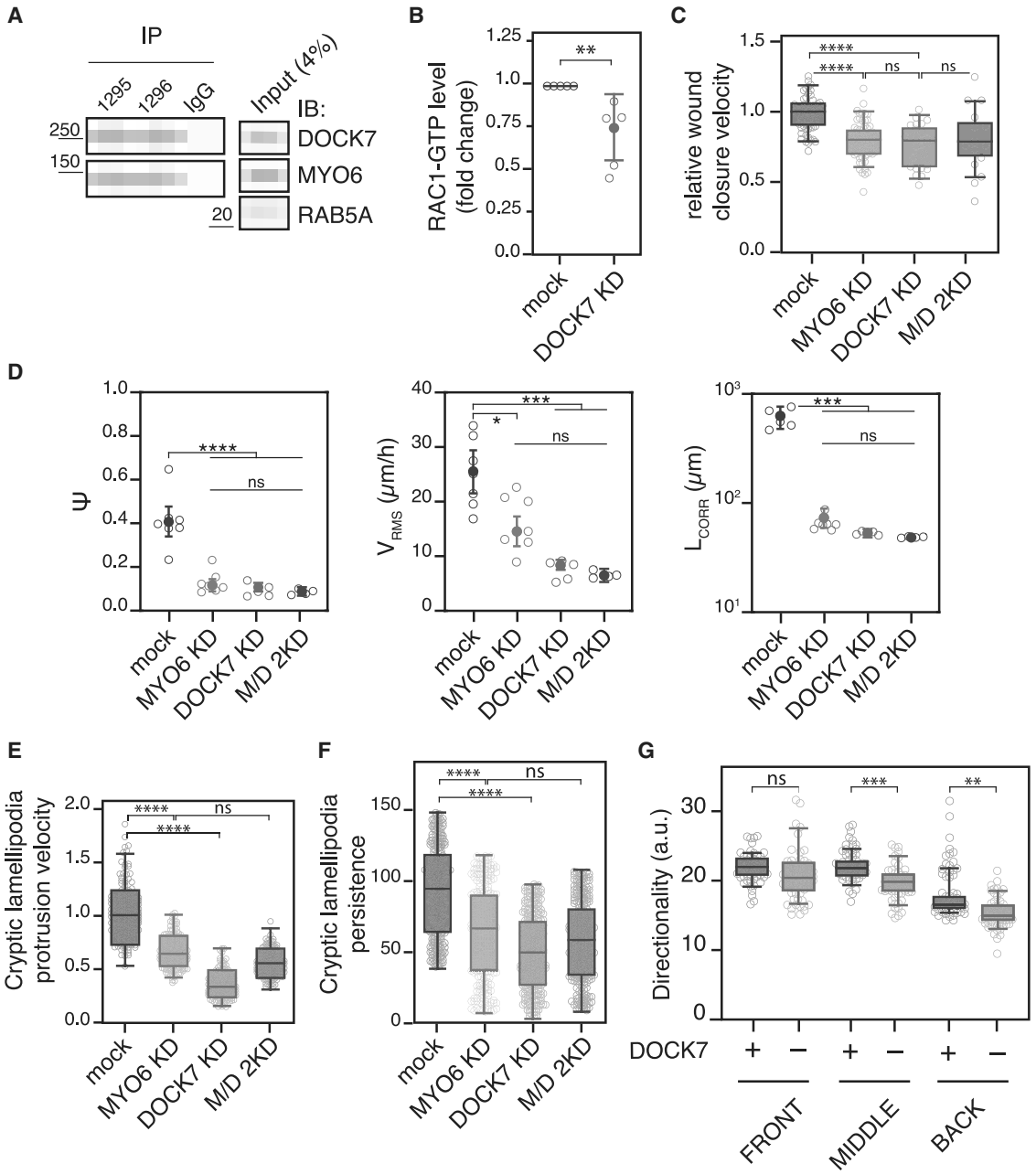

Figure 4. A MYO6-DOCK7 axis activates RAC1 in a planar polarized fashion

(A) Immunoprecipitation (IP) analysis of DCIS-RAB5A cells with two antibodies against myosin VI (1295 and 1296) and rabbit immunoglobulin G (IgG) as a negative control. IB as indicated.

(B) GST-CRIB assay quantification from mock or DOCK7 KD monolayers. Data are reported as fold change with respect to RAC1-GTP level in the corresponding mock sample for each experiment. n = 5 independent experiments. Reported values are mean ± SD. **p < 0.01 by Student's t test.

(C) Wound healing assay results for mock, MYO6 KD, DOCK7 KD, and the combination of MYO6- and DOCK7-depleted (M/D 2KD) cells. The average wound closure speed relative to the mock condition is plotted in the graph. The empty circle represents the mean wound closure velocity quantified for each video. n ≥ 15 (3 independent experiments). ns > 0.999, ****p < 0.0001 by ANOVA.

(D) PIV analysis of the streaming of the indicated cell monolayers. From left to right: orientational order parameter ψ, root-mean-squared velocity V_{RMS}, and correlation length L_{CORR}. The corresponding average stretching exponent β is 0.68 ± 0.1, 0.74 ± 0.06, 0.84 ± 0.07, and 0.87 ± 0.1 for mock, MYO6 KD, DOCK7 KD, and M/D 2KD, respectively. Empty circle, mean of each experiment calculated from five videos/condition (six independent experiments). Error bars ±SD. ns > 0.999, *p < 0.05, ***p < 0.001, ****p < 0.0001 by ANOVA.

(E) Quantification of cryptic lamellipodium protrusion velocity performed as in Figure 2D for the indicated cell lines. n = 158 (4 independent experiments).

(legend continued on next page)

interactome, which we identified in a previous study.[25] Among the myosin VI interactors, we focused on the human dedicator of cytokinesis DOCK7,[31,44,45] a dual guanine nucleotide exchange factor (GEF) for RAC1 and CDC42 GTPase.[46] We first confirmed that myosin VI and DOCK7 co-immunoprecipitated in DCIS-RAB5A cells (Figure 4A). Next, we tested the functional involvement of DOCK7 in regulation of RAC1 activity in cryptic lamellipodia in our model of flocking fluid motility in monolayers.

Biochemically, DOCK7 depletion significantly reduced RAC1-GTP levels (Figure 4B). Functionally, DOCK7 KD cells showed impaired collective migration in wound healing (Figure 4C; Video S9) and streaming assays (Figure 4D Video S10) to the same extent as in myosin VI KD cells. Intriguingly, concomitant silencing of DOCK7 and myosin VI did not worsen the migratory defects, suggesting that DOCK7 is likely the main effector of myosin VI activity in this context (Figures 4C and 4D). The results were confirmed by a second siRNA DOCK7 oligo (Figures S4A and S4B).

Next, we tested whether DOCK7-dependent impairment of flocking monolayer migration was due to a lack of oriented and persistent cryptic lamellipodia. By exploiting EGFP-LifeAct mosaic cells in confluent monolayers, we discovered that protrusion velocity and persistence of cryptic lamellipodia are similarly impaired after individual or concomitant depletion of DOCK7 and myosin VI (M/D 2KD) (Figures 4E and 4F). We then used cell segmentation and tracking of H2B-mCherry-labeled monolayer cells in a wound healing assay to specifically analyze migration of the leader or follower cells. Consistent with data obtained in myosin VI KD cells (Figures 2G–2I), silencing of DOCK7 did not affect the lamellipodium dynamics of the cell leading edge at the wound front (Figures S4C and S4D), while kymograph-based quantification of follower cells showed a significant reduction in directionality (Figure 4G).

Prompted by these results, we reasoned that myosin VI may be required to localize DOCK7 and spatially restrict its activity toward RAC1. To test this hypothesis, we first examined DOCK7 localization in our cell system. To overcome the lack of reliable antibodies, we generated a population of EGFP-DOCK7 cells that expressed low physiological levels of the protein (Figure S4E). A confocal analysis demonstrated that, in a confluent monolayer, DOCK7 co-localized with myosin VI at apical cell-cell junctions (Figure 5A) and accumulated in cryptic lamellipodia extending basally onto the cell substrate (Figures 5B and 5C). This localization requires myosin VI because, upon myosin VI depletion, DOCK7 became diffusely distributed throughout the cytoplasm (Figure 5D) and was no longer enriched at actin-rich protrusion tips (Figures 5E and 5F).

Collectively, these data indicate that a myosin VI-DOCK7-RAC1 axis controls cryptic lamellipodium protrusions, which, in turn, are required for collective flocking locomotion.

Myosin VI directly interacts with the DOCK7 DHR2 domain

A functional interaction between myosin VI and DOCK7 has been reported previously in the neuronal context[47] as well as in HeLa[44] and HEK293T cells,[31] but the molecular basis of this interaction has not been fully explored. Structurally, both proteins are composed of several distinct domains we investigated to map the critical surface of interaction (Figure S5A). First, we confirmed that the myosin VI binding surface resides in the DHR2 domain of DOCK7[45] because removal of this GEF catalytic domain in the context of the full-length protein was sufficient to abrogate binding to the myosin VI tail (Figure 6A). To identify the minimal binding region within myosin VI, we performed a pull-down experiment with different myosin VI tail constructs. The cargo-binding domain (CBD,[44]) and the MYO6 ubiquitin-binding (MyUb[48]) isolated domains bound DOCK7, although with reduced efficiency compared with the MyUb-CBD tail of myosin VI (Figure S5B). Importantly, using bacterially expressed and purified fragments, we showed that the interaction between the DHR2 domain and the MyUb-CBD domain is direct (Figure 6B).

The DOCK family consists of 11 structurally conserved proteins that serve as atypical RHO GEFs and are differentially expressed in tissues.[49,50] We tested the ability of the MyUb-CBD tail to bind the DHR2 domain of a few prototypes of the family, including DOCK2, DOCK6, and DOCK9.[51] Surprisingly, binding was detected only for the DHR2 domain of DOCK7 (Figure 6C).

This result prompted us to further analyze the interaction surface. Despite low sequence homology among the DOCK family members, the DHR2 domains are well conserved and adopt a similar fold that is characterized by three lobes, A–C. Of them, lobes B and C are endowed with GTPase binding and GEF activity, whereas lobe A seems to be involved in homodimerization, at least in a few DOCK proteins.[49,51] By using DHR2 protein fragments, we showed that lobe A is indeed required for DOCK7 dimerization but is also critical for myosin VI interaction (Figure S5B). Lobe A is not present in the recombinant DHR2 constructs used to generate the structural data for DOCK7 (PDB: 6AJ4). Therefore, we used AlphaFold2-Multimer[52,53] to predict the DOCK7 DHR2 structure and possible myosin VI interaction surfaces. The DOCK7 DHR2 and myosin VI MyUb and CBD domains were predicted with high confidence scores, except for a linker sequence between the two myosin VI domains that most likely is flexible (Figure 6D, top panel). The best model prediction indicated that the DOCK7 lobe A domain is in contact with the CBD and MyUb domains of myosin VI, with the MyUb and CBD domains also interacting with each other (Figure 6E). This model showed high confidence for the residue-to-residue distance (Figure 6D, bottom panel) and is fully consistent with the finding that loss of either MyUb or CBD weakens the interaction with DOCK7 (Figure S5B).

A hypothesis motivated by our structure-function analysis is that the binding of myosin VI to lobe A may influence the GEF activity of DOCK7. Indeed, DOCK7 showed poor activity on RAC1 compared with DOCK2 (Figure S5C), as reported previously,[46] strongly suggesting a possible allosteric missing partner. We

(F) Quantification of cryptic lamellipodium protrusion persistence performed as in Figure 2E for the indicated cell lines. n = 250 (4 independent experiments). ns > 0.999, ****p < 0.0001 by ANOVA.

(G) Quantification of the directionality of the cells belonging to the different areas performed as in Figure 2J for the indicated cell lines. n ≥ 34 (3 independent experiments). Error bars, ±SEM. ns > 0.999, ****p < 0.0001 by ANOVA.

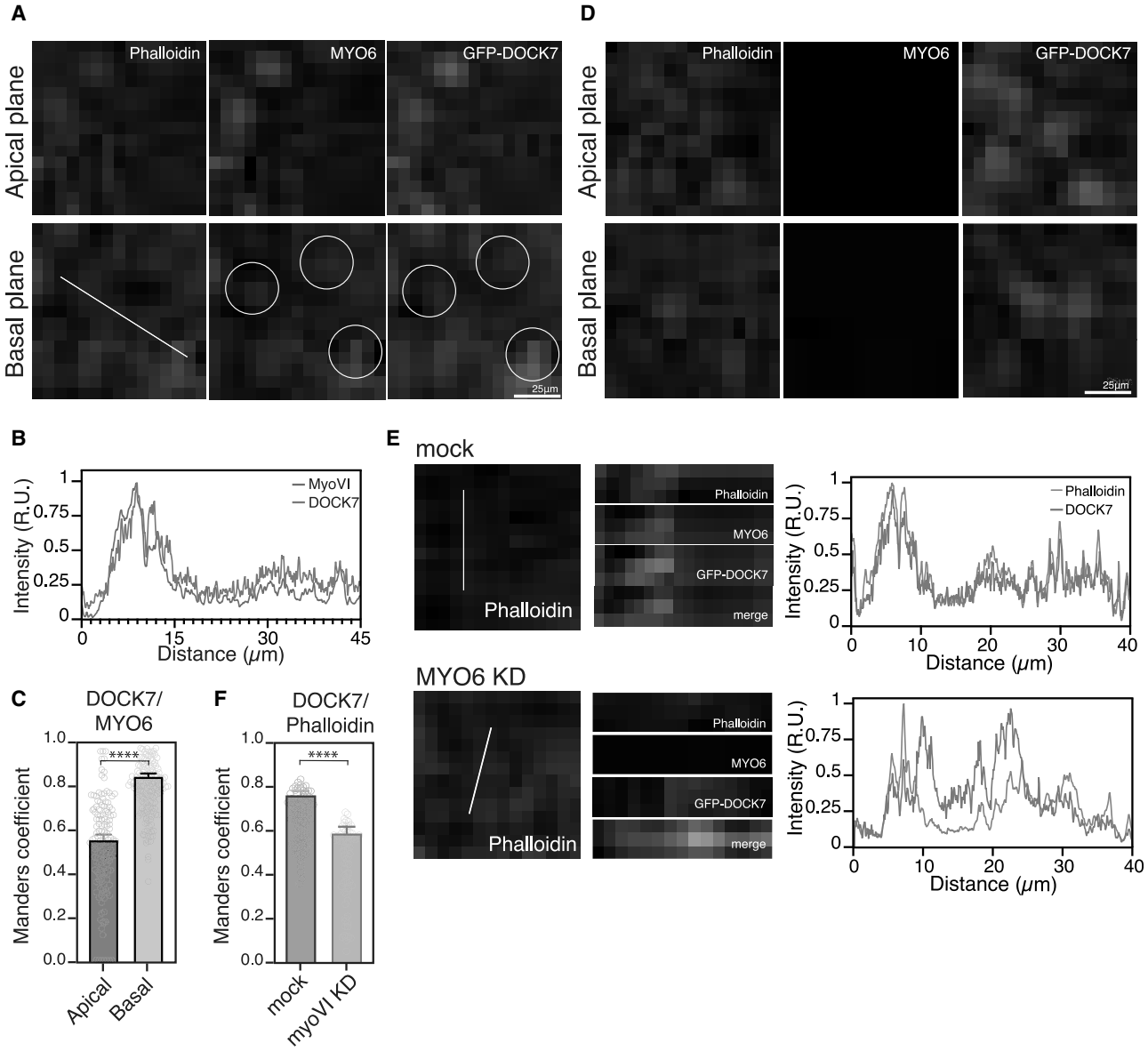

Figure 5. Myosin VI promotes local RAC1 activation by recruiting DOCK7 to cryptic lamellipodia

(A) IF analysis of GFP-DOCK7 expressing DCIS-RAB5A cells seeded in the jammed condition to visualize lamellipodium-like structures. Purple, myosin VI; red, phalloidin. Middle and basal planes are shown. Scale bars, 25 μm.

(B) Fluorescence intensity profiles show GFP-DOCK7 and MYO6 fluorescence distribution across the white line shown in (A) (x axis). The fluorescence intensities are reported on the y axis.

(C) Quantification of the colocalization of GFP-DOCK7 and myosin VI shown in (A), using Manders' coefficient. n = 153 (4 independent experiments). Error bars, ±SEM. ****p < 0.0001 by Student's t test.

(D) IF analysis of GFP-DOCK7 expressing DCIS-RAB5A cells depleted of myosin VI and seeded in the jammed condition as in (A). Purple, myosin VI; red, phalloidin. Middle and basal planes are shown.

(E) Z stacks acquisition of the cell lines described in (A) and (D). Right: fluorescence intensity profiles showing the distribution of GFP-DOCK 7 and phalloidin fluorescence across the white line (x axis).

(F) Quantification of the colocalization of GFP-DOCK7 and phalloidin in XZ images shown in (E), using Manders' coefficient. n ≥ 74 (four independent experiments). Error bars, ±SEM. ****p < 0.0001 by Student's t test.

then used a suboptimal concentration of DOCK7 and titrated in increasing amounts of the MyUb-CBD tail (Figure 6F), analyzing activity by the GEF assay. Even under these conditions, however, we failed to detect any effect of the MyUb-CBD fragment on the GEF activity of DOCK. Thus, we conclude that, while critical for DOCK7 localization, myosin VI does not appear to influence DOCK7 GEF activity toward RAC1, at least in this simplified *in vitro* experiment.

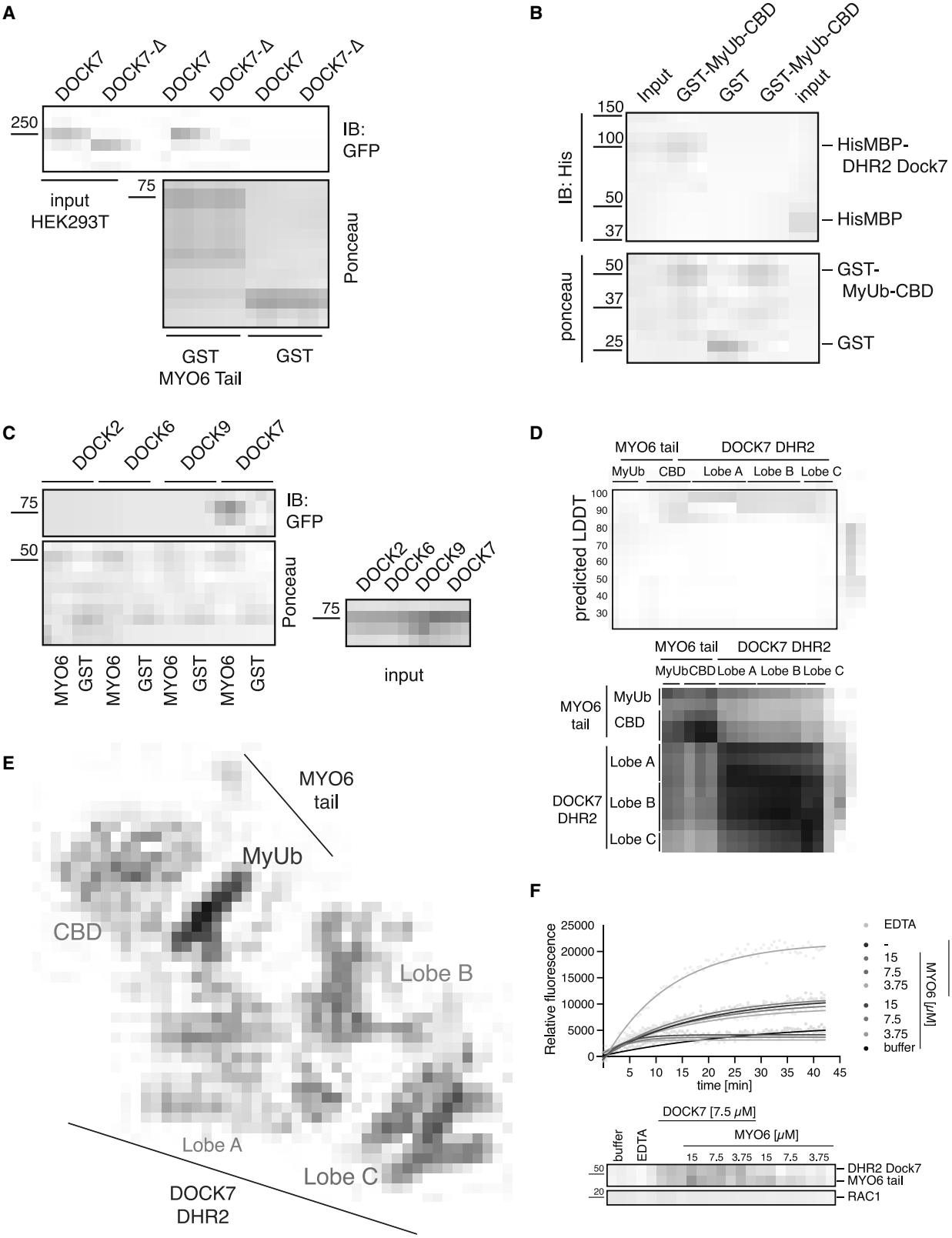

(legend on next page)

Myosin VI overexpression is exploited by infiltrating breast cancer cells

To assess the clinical relevance of our findings, we investigated the expression profile of myosin VI in human breast cancer by analyzing RNA sequencing (RNA-seq) data of The Cancer Genome Atlas (TCGA) breast tumors dataset (breast cancer [BRCA]). We assessed a total of 981 samples with complete clinical and pathological information, including molecular subtyping,[54] and we focused our attention on the myosin VI short isoform because we have demonstrated previously that this isoform is selectively required for cancer cell migration and for DOCK7 binding.[31] As shown in Figure 7A, expression of the myosin VI short isoform is significantly higher in the basal-like subtype compared with all other cancer subtypes and normal breast tissue. Notably, this subtype comprises 15%–20% of all breast tumors and largely correspond to triple-negative (TN) highly metastatic breast cancer, to which the MCF10.DCIS.com cell line belongs.

To confirm this result at the protein level, we analyzed a panel of human DCIS and invasive ductal carcinoma (IDC) tissue sections by immunohistochemistry. While diffuse and weak expression of myosin VI characterized most DCIS samples, the staining intensity was significantly higher in IDC, particularly in the infiltrating components (Figure 7B), as quantified by software analysis on digital slide scans (Figure 7C). Thus, breast carcinoma selectively increases myosin VI expression during progression from DCIS to IDC.

DISCUSSION

During carcinoma dissemination, cellular rearrangements are fostered by a solid-to-liquid transition, known as unjamming, through partially identified molecular mechanisms. We found here that myosin VI is essential to support this tissue-level phase transition because its depletion severely reduces cell coordination and impairs cell migration persistence and directionality. Molecularly, we identified DOCK7, a GEF for RAC1, as the critical and direct myosin VI interactor. Myosin VI is essential to restrict DOCK7 at cryptic lamellipodia to locally activate RAC1 and promote coordinated movement of the follower cells. This regulation may likely aid the follower cells to chase and coordinate their motion with the leaders, as recently suggested by several studies,[55,56] thereby enabling maintenance of monolayer compactness during collective motion. Our results also highlight the role exerted by RAC1 in the follower cells and show that these cells are not simply hitchhikers or passive passengers but, rather, actively contribute to promoting collective cell migration.

Our study has striking similarities with recent discoveries obtained in *Drosophila* by Campanale et al.,[55] who uncovered the role of a Scrib/Cdep/Rac pathway as essential for follower cell movement and cluster cohesion in border cell migration. In this study and context, Cdep was identified as the Rac GEF, whereas Scrib, Dlg, and Lgl aid in localizing Cdep basolaterally to activate Rac in followers. Intriguingly, *Drosophila* was the system first employed to demonstrate the critical role of myosin VI in collective motion because its depletion severely affects border cell migration.[27] Whether myosin VI does so by perturbing RAC1 activity in follower cells in conjunction with or alternatively to Scrib and Cdep has not been addressed. Likely, more than a RacGEF is required in follower cells, and little is known about the DOCK7 ortholog in *Drosophila*, Zir. Thus, it will be exciting to re-evaluate the role of myosin VI and Zir activity in border cell dynamics in light of our current finding.

It must be noted that border cells display not only a leader-to-follower topological organization but also an apicobasal polarity during their motion, consistent with their prototypical epithelial nature. Conversely, breast carcinoma MCF10.DCIS.com cells nearly completely lose their apico-basal polarity while they retain a number of features of normal epithelial tissues, including a planar polarized organization. Because the molecular determinants of these polarity programs are distinct, it is conceivable that myosin VI might be more critical when a planar polarity arrangement is needed and established but dispensable during apico-basal organization. This specific role is particularly attractive considering the selective role exerted by the alternatively spliced myosin VI isoforms.[25,31] Indeed, fully polarized epithelia selectively express myosin VI long, which is impaired in DOCK7 binding[31] and is critical for clathrin-mediated endocytosis at the apical surface.[57]

Limitations of the study

Our findings imply that the myosin VI short isoform is relevant for infiltrating carcinoma cells to ensure and enhance coordinated and directed collective invasion during unjamming. Although several lines of evidence support this idea, investigation of myosin VI isoforms has been limited to mRNA expression analysis because of the unavailability of isoform-specific antibodies for protein detection. Therefore, further investigations are needed to determine the spatial and temporal expression of the short isoform protein in different tumor subtypes. Moreover,

Figure 6. Myosin VI specifically and directly interacts with the lobe A of the DHR2 domain of DOCK7

(A) GST pull-down assay using the myosin VI tail and lysates from HEK293T cells transfected with full-length GFP-DOCK7 or its DHR2 deleted mutant, GFP-DOCK7ΔDHR2 (DOCK7Δ). IB as indicated. Ponceau shows equal loading.

(B) Pull-down assay using the HisMBP-DHR2 domain of DOCK7 and MyUb-CBD construct of myosin VI produced and purified from bacteria. IB as indicated. Ponceau shows equal loading.

(C) GST pull-down assay using MyUb-CBD of myosin VI (spanning amino acids 1,080–1,295) and lysate from HEK293T cells transfected with the GFP-DHR2 domain of the indicated DOCK proteins. IB as indicated. Ponceau shows equal loading.

(D) Confidence scores per residue generated by AlphaFold2-Multimer for the predicted fold of domains (top) and the residue-to-residue distance (bottom). LDDT, local distance difference test.

(E) Ribbon diagram of the top-scoring AlphaFold2-Multimer model of the MYO6:DOCK7 interaction obtained by entering protein sequences for the myosin VI tail, spanning residues G1048–K1262, and DOCK7 residues of the DHR2 domain spanning P775–P1196.

(F) Representative RAC1 GEF activity assay using 7.5 μM of the DHR2 domain of DOCK7 and the indicated concentration of the MyUb-CBD myosin VI. Bottom: Coomassie gel of the samples used.

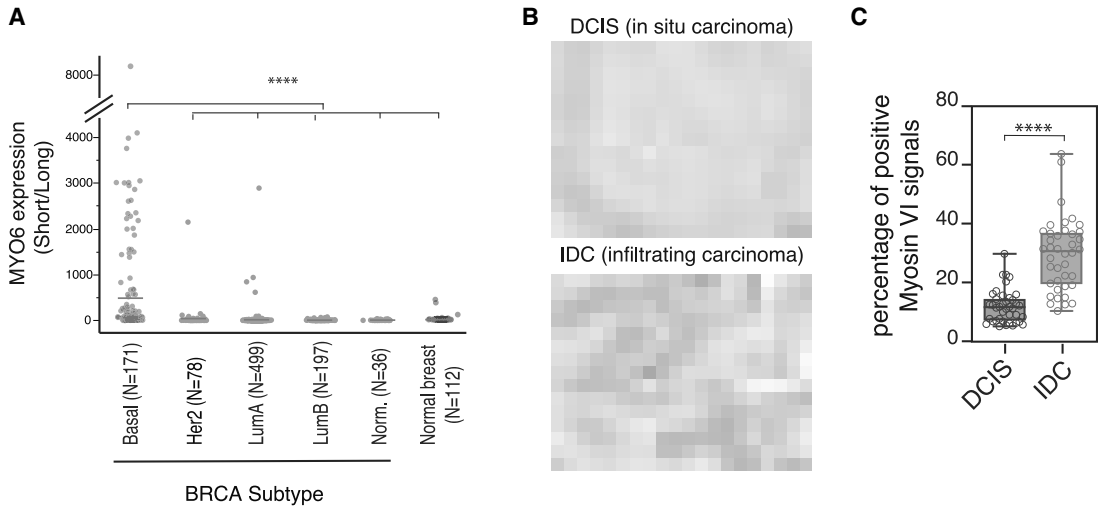

Figure 7. MYO6 is significantly overexpressed in highly metastatic breast cancers

(A) MYO6 short versus long isoform expression expressed as ratio of RPKM (reads per kilobase per million mapped reads) for the indicated BRCA subtypes. Average expression level is shown by green lines. The myosin VI short isoform was significantly overexpressed in the BRCA basal-like subtype compared with all other subtypes and normal breast tissues. Statistical significance was analyzed by one-way (chi-square approximation) Wilcoxon test. ***$p < 0.0001$.

(B) Representative immunohistochemistry (IHC) images of myosin VI in DCIS and IDC tumor sections. Original magnification, ×200. Scale bar, 100 μm.

(C) Quantitative analyses of myosin VI IHC images shown in (B). n = 40 (5 images of 8 cases/cancer type). ****$p < 0.0001$ by Student's t test.

while our results indicate that the alteration of alternative splicing mechanism of myosin VI is selected during cancer progression, the underlying process still requires clarification.

While we discovered the MYO6-DOCK7-RAC1 axis in the MCF10.DCIS.com cell line, which is representative of basal-like breast cancers, its applicability in different cellular contexts as well as murine models of breast cancer requires further investigation. To gain a comprehensive understanding of the system and establish the therapeutic potential of this critical molecular axis, further *in vitro* and *in vivo* studies are necessary. Notably, while direct inhibition of myosin VI may have unwanted deleterious effects in normal tissues,[58] the interaction surface with DOCK7 represents a promising possibility to explore in future drug discovery studies, particularly in the case of the more aggressive basal-like breast cancers for which we have limited therapeutic options.

STAR★METHODS

Detailed methods are provided in the online version of this paper and include the following:

- KEY RESOURCES TABLE
- RESOURCE AVAILABILITY
  - Lead contact
  - Materials availability
  - Data and code availability
- METHOD DETAILS
  - Constructs and reagents
  - Cell lines and transfection procedures
  - Antibodies
  - Single cell migration assay
  - Wound healing assays
  - Measurement of the cellular velocities and trajectories
  - Kymograph analysis of cell protrusions at the wound edge
  - Cell sheet streaming and kinetic parameter measurements
  - Measurements of cryptic lamellipodia dynamics
  - Immunofluorescence (IF)
  - FRET based RAC1/CDC42 activation assay
  - Protein expression and purification
  - Co-immunoprecipitation and pull-down assays
  - AlphaFold2-multimer prediction
  - GEF activity assay
  - IHC analysis and quantification
  - Expression profile analysis
- QUANTIFICATION AND STATISTICAL ANALYSIS

SUPPLEMENTAL INFORMATION

Supplemental information can be found online at https://doi.org/10.1016/j.celrep.2023.113001.

ACKNOWLEDGMENTS

We are grateful to all members of the IFOM imaging facility, in particular Francesca Casagrande, Serena Magni, and Zeno Lavagnino for support with image acquisition and analysis and Maria Grazia Totaro for support with cell sorting. This work was supported by the Associazione Italiana per Ricerca sul Cancro (investigator grant 2017-19875 to S.P., 2019-18621 and 5Xmille 22759 to G.S., and My First AIRC grant 2018-22083 to F.G.); the Seal of Excellence (SoE SEED2020 to S.P. and F.G.); the Intramural Research Program through the Center for Cancer Research, National Cancer Institute, National Institutes of Health (ZIA BC011627 to K.J.W.); and the European Union (ERC, ShapinCellFate, 101071470 to G.S.). The views and opinions expressed are, however, those of the author(s) only and do not necessarily reflect those of the European Union or the European Research Council Executive Agency. Neither the

European Union nor the granting authority can be held responsible for them. AlphaFold2-Multimer was run using computational resources of the High-Performance Computing Biowulf cluster of the NIH (http://hpc.nih.gov). L.M.'s work was supported by a fellowship of the Associazione Italiana per Ricerca sul Cancro. The graphical abstract was generated with BioRender.

AUTHOR CONTRIBUTIONS

Conceptualization, L.M., G.S., and S.P.; investigation, L.M. and J.W.; methodology, L.M., J.W., S.V., E. Maspero, C.A.N., V.C., A. Poli, P.M., A. Palanidessi., E.F., F.B., C.T., and K.J.W.; formal analysis, L.M., J.W., S.V., E. Martini, F.B., and K.J.W.; supervision, F.G., G.S., and S.P; data curation, L.M. and S.P.; writing – original draft, L.M. and S.P.; writing – review & editing, G.S. and S.P.; funding acquisition, S.P.

DECLARATION OF INTERESTS

The authors declare no competing interests.

INCLUSION AND DIVERSITY

We support inclusive, diverse, and equitable conduct of research.

Received: March 17, 2023
Revised: April 24, 2023
Accepted: August 1, 2023
Published: August 16, 2023

REFERENCES

1. Scarpa, E., and Mayor, R. (2016). Collective cell migration in development. J. Cell Biol. *212*, 143–155. https://doi.org/10.1083/jcb.201508047.
2. Haeger, A., Wolf, K., Zegers, M.M., and Friedl, P. (2015). Collective cell migration: guidance principles and hierarchies. Trends Cell Biol. *25*, 556–566. https://doi.org/10.1016/j.tcb.2015.06.003.
3. Friedl, P., and Wolf, K. (2010). Plasticity of cell migration: a multiscale tuning model. J. Cell Biol. *188*, 11–19. https://doi.org/10.1083/jcb.200909003.
4. Friedl, P., and Gilmour, D. (2009). Collective cell migration in morphogenesis, regeneration and cancer. Nat. Rev. Mol. Cell Biol. *10*, 445–457. https://doi.org/10.1038/nrm2720.
5. Barriga, E.H., Franze, K., Charras, G., and Mayor, R. (2018). Tissue stiffening coordinates morphogenesis by triggering collective cell migration in vivo. Nature *554*, 523–527. https://doi.org/10.1038/nature25742.
6. Qin, L., Yang, D., Yi, W., Cao, H., and Xiao, G. (2021). Roles of leader and follower cells in collective cell migration. Mol. Biol. Cell *32*, 1267–1272. https://doi.org/10.1091/mbc.E20-10-0681.
7. Szabó, B., Szöllösi, G.J., Gönci, B., Jurányi, Z., Selmeczi, D., and Vicsek, T. (2006). Phase transition in the collective migration of tissue cells: Experiment and model. Phys. Rev. *74*, 061908. https://doi.org/10.1103/PhysRevE.74.061908.
8. Angelini, T.E., Hannezo, E., Trepat, X., Marquez, M., Fredberg, J.J., and Weitz, D.A. (2011). Glass-like dynamics of collective cell migration. Proc. Natl. Acad. Sci. USA *108*, 4714–4719. https://doi.org/10.1073/pnas.1010059108.
9. Giavazzi, F., Paoluzzi, M., Macchi, M., Bi, D., Scita, G., Manning, M.L., Cerbino, R., and Marchetti, M.C. (2018). Flocking transitions in confluent tissues. Soft Matter *14*, 3471–3477. https://doi.org/10.1039/C8SM00126J.
10. Hakim, V., and Silberzan, P. (2017). Collective cell migration: a physics perspective. Rep. Prog. Phys. *80*, 076601. https://doi.org/10.1088/1361-6633/aa65ef.
11. Krause, M., and Gautreau, A. (2014). Steering cell migration: lamellipodium dynamics and the regulation of directional persistence. Nat. Rev. Mol. Cell Biol. *15*, 577–590. https://doi.org/10.1038/nrm3861.
12. Farooqui, R., and Fenteany, G. (2005). Multiple rows of cells behind an epithelial wound edge extend cryptic lamellipodia to collectively drive cell-sheet movement. J. Cell Sci. *118*, 51–63. https://doi.org/10.1242/jcs.01577.
13. Barlan, K., Cetera, M., and Horne-Badovinac, S. (2017). Fat2 and Lar Define a Basally Localized Planar Signaling System Controlling Collective Cell Migration. Dev. Cell *40*, 467–477.e5. https://doi.org/10.1016/j.devcel.2017.02.003.
14. Malinverno, C., Corallino, S., Giavazzi, F., Bergert, M., Li, Q., Leoni, M., Disanza, A., Frittoli, E., Oldani, A., Martini, E., et al. (2017). Endocytic reawakening of motility in jammed epithelia. Nat. Mater. *16*, 587–596. https://doi.org/10.1038/nmat4848.
15. Park, J.-A., Atia, L., Mitchel, J.A., Fredberg, J.J., and Butler, J.P. (2016). Collective migration and cell jamming in asthma, cancer and development. J. Cell Sci. *129*, 3375–3383. https://doi.org/10.1242/jcs.187922.
16. Frittoli, E., Palamidessi, A., Marighetti, P., Confalonieri, S., Bianchi, F., Malinverno, C., Mazzarol, G., Viale, G., Martin-Padura, I., Garré, M., et al. (2014). A RAB5/RAB4 recycling circuitry induces a proteolytic invasive program and promotes tumor dissemination. J. Cell Biol. *206*, 307–328. https://doi.org/10.1083/jcb.201403127.
17. Palamidessi, A., Malinverno, C., Frittoli, E., Corallino, S., Barbieri, E., Sigismund, S., Beznoussenko, G.V., Martini, E., Garre, M., Ferrara, I., et al. (2019). Unjamming overcomes kinetic and proliferation arrest in terminally differentiated cells and promotes collective motility of carcinoma. Nat. Mater. *18*, 1252–1263. https://doi.org/10.1038/s41563-019-0425-1.
18. Giavazzi, F., Malinverno, C., Corallino, S., Ginelli, F., Scita, G., and Cerbino, R. (2017). Giant fluctuations and structural effects in a flocking epithelium. J. Phys. D Appl. Phys. *50*, 384003. https://doi.org/10.1088/1361-6463/aa7f8e.
19. Ridley, A.J. (2015). Rho GTPase signalling in cell migration. Curr. Opin. Cell Biol. *36*, 103–112. https://doi.org/10.1016/j.ceb.2015.08.005.
20. Xi, W., Sonam, S., Beng Saw, T., Ladoux, B., and Teck Lim, C. (2017). Emergent patterns of collective cell migration under tubular confinement. Nat. Commun. *8*, 1517. https://doi.org/10.1038/s41467-017-01390-x.
21. Omelchenko, T., Vasiliev, J.M., Gelfand, I.M., Feder, H.H., and Bonder, E.M. (2003). Rho-dependent formation of epithelial "leader" cells during wound healing. Proc. Natl. Acad. Sci. USA *100*, 10788–10793. https://doi.org/10.1073/pnas.1834401100.
22. Gov, N.S. (2007). Collective cell migration patterns: Follow the leader. Proc. Natl. Acad. Sci. USA *104*, 15970–15971. https://doi.org/10.1073/pnas.0708037104.
23. Poujade, M., Grasland-Mongrain, E., Hertzog, A., Jouanneau, J., Chavrier, P., Ladoux, B., Buguin, A., and Silberzan, P. (2007). Collective migration of an epithelial monolayer in response to a model wound. Proc. Natl. Acad. Sci. USA *104*, 15988–15993. https://doi.org/10.1073/pnas.0705062104.
24. Sweeney, H.L., and Houdusse, A. (2007). What can myosin VI do in cells? Curr. Opin. Cell Biol. *19*, 57–66. https://doi.org/10.1016/j.ceb.2006.12.005.
25. Magistrati, E., and Polo, S. (2021). Myomics: myosin VI structural and functional plasticity. Curr. Opin. Struct. Biol. *67*, 33–40. https://doi.org/10.1016/j.sbi.2020.09.005.
26. Chibalina, M.V., Puri, C., Kendrick-Jones, J., and Buss, F. (2009). Potential roles of myosin VI in cell motility. Biochem. Soc. Trans. *37*, 966–970. https://doi.org/10.1042/BST0370966.
27. Geisbrecht, E.R., and Montell, D.J. (2002). Myosin VI is required for E-cadherin-mediated border cell migration. Nat. Cell Biol. *4*, 616–620. https://doi.org/10.1038/ncb830.
28. Yoshida, H., Cheng, W., Hung, J., Montell, D., Geisbrecht, E., Rosen, D., Liu, J., and Naora, H. (2004). Lessons from border cell migration in the Drosophila ovary: A role for myosin VI in dissemination of human ovarian cancer. Proc. Natl. Acad. Sci. USA *101*, 8144–8149. https://doi.org/10.1073/pnas.0400400101.

29. Dunn, T.A., Chen, S., Faith, D.A., Hicks, J.L., Platz, E.A., Chen, Y., Ewing, C.M., Sauvageot, J., Isaacs, W.B., De Marzo, A.M., and Luo, J. (2006). A novel role of myosin VI in human prostate cancer. Am. J. Pathol. *169*, 1843–1854. https://doi.org/10.2353/ajpath.2006.060316.

30. Wang, H., Wang, B., Zhu, W., and Yang, Z. (2015). Retracted: Lentivirus-Mediated Knockdown of Myosin VI Inhibits Cell Proliferation of Breast Cancer Cell. Cancer Biother. Radiopharm. *30*, 330–335. https://doi.org/10.1089/cbr.2014.1759.

31. Wollscheid, H.-P., Biancospino, M., He, F., Magistrati, E., Molteni, E., Lupia, M., Soffientini, P., Rottner, K., Cavallaro, U., Pozzoli, U., et al. (2016). Diverse functions of myosin VI elucidated by an isoform-specific α-helix domain. Nat. Struct. Mol. Biol. *23*, 300–308. https://doi.org/10.1038/nsmb.3187.

32. Acharya, B.R., Nestor-Bergmann, A., Liang, X., Gupta, S., Duszyc, K., Gauquelin, E., Gomez, G.A., Budnar, S., Marcq, P., Jensen, O.E., et al. (2018). A Mechanosensitive RhoA Pathway that Protects Epithelia against Acute Tensile Stress. Dev. Cell *47*, 439–452.e6. https://doi.org/10.1016/j.devcel.2018.09.016.

33. Maddugoda, M.P., Crampton, M.S., Shewan, A.M., and Yap, A.S. (2007). Myosin VI and vinculin cooperate during the morphogenesis of cadherin cell–cell contacts in mammalian epithelial cells. J. Cell Biol. *178*, 529–540. https://doi.org/10.1083/jcb.200612042.

34. Mangold, S., Norwood, S.J., Yap, A.S., and Collins, B.M. (2012). The juxtamembrane domain of the E-cadherin cytoplasmic tail contributes to its interaction with Myosin VI. BioArchitecture *2*, 185–188. https://doi.org/10.4161/bioa.22082.

35. Ozawa, M., Hiver, S., Yamamoto, T., Shibata, T., Upadhyayula, S., Mimori-Kiyosue, Y., and Takeichi, M. (2020). Adherens junction regulates cryptic lamellipodia formation for epithelial cell migration. J. Cell Biol. *219*, e202006196. https://doi.org/10.1083/jcb.202006196.

36. Grützmacher, S., Kemkemer, R., Thies, C., and Curio, C. (2018). Detecting Lamellipodia in Epithelial Cell Clusters Using a Fully Convolutional Neural Network for Phase Contrast. Microscopy Images *4*, 449–452. https://doi.org/10.1515/cdbme-2018-0107.

37. Fritz, R.D., Menshykau, D., Martin, K., Reimann, A., Pontelli, V., and Pertz, O. (2015). SrGAP2-Dependent Integration of Membrane Geometry and Slit-Robo-Repulsive Cues Regulates Fibroblast Contact Inhibition of Locomotion. Dev. Cell *35*, 78–92. https://doi.org/10.1016/j.devcel.2015.09.002.

38. Remorino, A., De Beco, S., Cayrac, F., Di Federico, F., Cornilleau, G., Gautreau, A., Parrini, M.C., Masson, J.-B., Dahan, M., and Coppey, M. (2017). Gradients of Rac1 Nanoclusters Support Spatial Patterns of Rac1 Signaling. Cell Rep. *21*, 1922–1935. https://doi.org/10.1016/j.celrep.2017.10.069.

39. Das, S., Yin, T., Yang, Q., Zhang, J., Wu, Y.I., and Yu, J. (2015). Single-molecule tracking of small GTPase Rac1 uncovers spatial regulation of membrane translocation and mechanism for polarized signaling. Proc. Natl. Acad. Sci. USA *112*, E267–E276. https://doi.org/10.1073/pnas.1409667112.

40. Martin, K., Reimann, A., Fritz, R.D., Ryu, H., Jeon, N.L., and Pertz, O. (2016). Spatio-temporal co-ordination of RhoA, Rac1 and Cdc42 activation during prototypical edge protrusion and retraction dynamics. Sci. Rep. *6*, 21901. https://doi.org/10.1038/srep21901.

41. Levay, M., Krobert, K.A., Wittig, K., Voigt, N., Bermudez, M., Wolber, G., Dobrev, D., Levy, F.O., and Wieland, T. (2013). NSC23766, a Widely Used Inhibitor of Rac1 Activation, Additionally Acts as a Competitive Antagonist at Muscarinic Acetylcholine Receptors. J. Pharmacol. Exp. Therapeut. *347*, 69–79. https://doi.org/10.1124/jpet.113.207266.

42. Kai, Y., Motegi, M., Suzuki, Y., Harada, Y., Takeuchi, H., Kon, R., Ikarashi, N., Chiba, Y., Kamei, J., and Sakai, H. (2019). Increased Rac1 Activation in the Enhanced Carbachol-Induced Bronchial Smooth Muscle Contraction of Repeatedly Antigen-Challenged Mice. Biol. Pharm. Bull. *42*, 1605–1607. https://doi.org/10.1248/bpb.b19-00404.

43. Davis, M.J., Ha, B.H., Holman, E.C., Halaban, R., Schlessinger, J., and Boggon, T.J. (2013). RAC1^{P29S} is a spontaneously activating cancer-associated GTPase. Proc. Natl. Acad. Sci. USA *110*, 912–917. https://doi.org/10.1073/pnas.1220895110.

44. O'Loughlin, T., Masters, T.A., and Buss, F. (2018). The MYO6 interactome reveals adaptor complexes coordinating early endosome and cytoskeletal dynamics. EMBO Rep. *19*, e44884. https://doi.org/10.15252/embr.201744884.

45. Sobczak, M., Chumak, V., Pomorski, P., Wojtera, E., Majewski, Ł., Nowak, J., Yamauchi, J., and Rędowicz, M.J. (2016). Interaction of myosin VI and its binding partner DOCK7 plays an important role in NGF-stimulated protrusion formation in PC12 cells. Biochim. Biophys. Acta *1863*, 1589–1600. https://doi.org/10.1016/j.bbamcr.2016.03.020.

46. Kukimoto-Niino, M., Tsuda, K., Ihara, K., Mishima-Tsumagari, C., Honda, K., Ohsawa, N., and Shirouzu, M. (2019). Structural Basis for the Dual Substrate Specificity of DOCK7 Guanine Nucleotide Exchange Factor. Structure *27*, 741–748.e3. https://doi.org/10.1016/j.str.2019.02.001.

47. Majewski, Ł., Sobczak, M., Havrylov, S., Jóźwiak, J., and Rędowicz, M.J. (2012). Dock7: A GEF for Rho-family GTPases and a novel myosin VI-binding partner in neuronal PC12 cells. Biochem. Cell. Biol. *90*, 565–574. https://doi.org/10.1139/o2012-009.

48. He, F., Wollscheid, H.-P., Nowicka, U., Biancospino, M., Valentini, E., Ehlinger, A., Acconcia, F., Magistrati, E., Polo, S., and Walters, K.J. (2016). Myosin VI Contains a Compact Structural Motif that Binds to Ubiquitin Chains. Cell Rep. *14*, 2683–2694. https://doi.org/10.1016/j.celrep.2016.01.079.

49. Laurin, M., and Côté, J.F. (2014). Insights into the biological functions of Dock family guanine nucleotide exchange factors. Genes Dev. *28*, 533–547. https://doi.org/10.1101/gad.236349.113.

50. Côté, J.F., and Vuori, K. (2002). Identification of an evolutionarily conserved superfamily of DOCK180-related proteins with guanine nucleotide exchange activity. J. Cell Sci. *115*, 4901–4913. https://doi.org/10.1242/jcs.00219.

51. Kulkarni, K., Yang, J., Zhang, Z., and Barford, D. (2011). Multiple Factors Confer Specific Cdc42 and Rac Protein Activation by Dedicator of Cytokinesis (DOCK) Nucleotide Exchange Factors. Journal of Biological Chemistry *286*, 25341–25351. https://doi.org/10.1074/jbc.M111.236455.

52. Jumper, J., Evans, R., Pritzel, A., Green, T., Figurnov, M., Ronneberger, O., Tunyasuvunakool, K., Bates, R., Žídek, A., Potapenko, A., et al. (2021). Highly accurate protein structure prediction with AlphaFold. Nature *596*, 583–589. https://doi.org/10.1038/s41586-021-03819-2.

53. Tunyasuvunakool, K., Adler, J., Wu, Z., Green, T., Zielinski, M., Žídek, A., Bridgland, A., Cowie, A., Meyer, C., Laydon, A., et al. (2021). Highly accurate protein structure prediction for the human proteome. Nature *596*, 590–596. https://doi.org/10.1038/s41586-021-03828-1.

54. Cancer Genome Atlas Network (2012). Comprehensive molecular portraits of human breast tumours. Nature *490*, 61–70. https://doi.org/10.1038/nature11412.

55. Campanale, J.P., Mondo, J.A., and Montell, D.J. (2022). A Scribble/Cdep/Rac pathway controls follower-cell crawling and cluster cohesion during collective border-cell migration. Dev. Cell *57*, 2483–2496.e4. https://doi.org/10.1016/j.devcel.2022.10.004.

56. Vishwakarma, M., Di Russo, J., Probst, D., Schwarz, U.S., Das, T., and Spatz, J.P. (2018). Mechanical interactions among followers determine the emergence of leaders in migrating epithelial cell collectives. Nat. Commun. *9*, 3469. https://doi.org/10.1038/s41467-018-05927-6.

57. Biancospino, M., Buel, G.R., Niño, C.A., Maspero, E., Scotto di Perrotolo, R., Raimondi, A., Redlingshöfer, L., Weber, J., Brodsky, F.M., Walters, K.J., and Polo, S. (2019). Clathrin light chain A drives selective myosin VI recruitment to clathrin-coated pits under membrane tension. Nat. Commun. *10*, 4974. https://doi.org/10.1038/s41467-019-12855-6.

58. Magistrati, E., Maestrini, G., Niño, C.A., Lince-Faria, M., Beznoussenko, G., Mironov, A., Maspero, E., Bettencourt-Dias, M., and Polo, S. (2022).

Myosin VI regulates ciliogenesis by promoting the turnover of the centrosomal/satellite protein OFD1. EMBO Rep. *23*, e54160. https://doi.org/10.15252/embr.202154160.

59. Innocenti, M., Tenca, P., Frittoli, E., Faretta, M., Tocchetti, A., Di Fiore, P.P., and Scita, G. (2002). Mechanisms through which Sos-1 coordinates the activation of Ras and Rac. J. Cell Biol. *156*, 125–136. https://doi.org/10.1083/jcb.200108035.

60. Thielicke, W., and Sonntag, R. (2021). Particle Image Velocimetry for MATLAB: Accuracy and enhanced algorithms in PIVlab. J. Open Res. Software *9*, 12. https://doi.org/10.5334/jors.334.

61. Sun, W., Duan, T., Ye, P., Chen, K., Zhang, G., Lai, M., and Zhang, H. (2018). TSVdb: a web-tool for TCGA splicing variants analysis. BMC Genom. *19*, 405. https://doi.org/10.1186/s12864-018-4775-x.

62. Nakamuta, S., Yang, Y.-T., Wang, C.-L., Gallo, N.B., Yu, J.-R., Tai, Y., and Van Aelst, L. (2017). Dual role for DOCK7 in tangential migration of interneuron precursors in the postnatal forebrain. J. Cell Biol. *216*, 4313–4330. https://doi.org/10.1083/jcb.201704157.

63. Palamidessi, A., Frittoli, E., Garré, M., Faretta, M., Mione, M., Testa, I., Diaspro, A., Lanzetti, L., Scita, G., and Di Fiore, P.P. (2008). Endocytic Trafficking of Rac Is Required for the Spatial Restriction of Signaling in Cell Migration. Cell *134*, 135–147. https://doi.org/10.1016/j.cell.2008.05.034.

64. Nastały, P., Purushothaman, D., Marchesi, S., Poli, A., Lendenmann, T., Kidiyoor, G.R., Beznoussenko, G.V., Lavore, S., Romano, O.M., Poulikakos, D., et al. (2020). Role of the nuclear membrane protein Emerin in front-rear polarity of the nucleus. Nat. Commun. *11*, 2122. https://doi.org/10.1038/s41467-020-15910-9.

65. Villa, S., Palamidessi, A., Frittoli, E., Scita, G., Cerbino, R., and Giavazzi, F. (2022). Non-invasive measurement of nuclear relative stiffness from quantitative analysis of microscopy data. Eur. Phys. J. E Soft Matter *45*, 50. https://doi.org/10.1140/epje/s10189-022-00189-z.

66. Crocker, J.C., and Grier, D.G. (1996). Methods of Digital Video Microscopy for Colloidal Studies. J. Colloid Interface Sci. *179*, 298–310. https://doi.org/10.1006/jcis.1996.0217.

67. Bolte, S., and Cordelières, F.P. (2006). A guided tour into subcellular colocalization analysis in light microscopy. J. Microsc. *224*, 213–232. https://doi.org/10.1111/j.1365-2818.2006.01706.x.

68. Manders, E.M.M., Verbeek, F.J., and Aten, J.A. (1993). Measurement of co-localization of objects in dual-colour confocal images. J. Microsc. *169*, 375–382. https://doi.org/10.1111/j.1365-2818.1993.tb03313.x.

STAR★METHODS

KEY RESOURCES TABLE

REAGENT or RESOURCE	SOURCE	IDENTIFIER
Antibodies		
anti-Desmoplakin	provided by Kathleen Green	N/A
anti-RAC1	Becton Dickinson	Cat#610651
anti-MYO6	Wollscheid et al.[31]	Eurogentec-1296
anti-GAPDH	Santa Cruz	Cat#32233
anti-DOCK7	Santa Cruz	Cat#398888
anti-RAB5A	Santa Cruz	Cat#166600
anti-CDC42	Santa Cruz	Cat#390210
anti-GFP	Sigma-Aldrich	Cat#G1544
anti-His	Cell Signaling	Cat#2366
Chemicals, peptides, and recombinant proteins		
Human EGF	Vinci Biochem	BPS-90201-1
GST-beads	GE Healthcare	GE17-0756-01
GFP-TRAP	Cromotek	RRID: AB_2631357
BODIPY^{TM} FL-GTP	Thermo Fisher Scientific	Cat# G12411
Carbachol	Calbiochem, Sigma	CAS 51-83-2
Deposited data		
Raw and analyzed data	This study, Mendeley Data	https://doi.org/10.17632/zsxcs45pt3.1
TCGA-BRCA	https://portal.gdc.cancer.gov/projects/TCGA-BRCA	phs000178
Experimental models: Cell lines		
MCF10.DCIS.com RAB5A	Malinverno et al.[14]	N/A
MCF10.DCIS.com RAB5A GFP-LifeAct mCherry-H2B	Malinverno et al.[14]	N/A
MCF10.DCIS.com RAB5A mCherry-H2B	Malinverno et al.[14]	N/A
MCF10.DCIS.com RAB5A GFP-DOCK7	This study	N/A
MCF10.DCIS.com RAB5A GFP-LifeAct mCherry-H2B RAC1 WT	This study	N/A
MCF10.DCIS.com RAB5A GFP-LifeAct mCherry-H2B RAC1 P62S	This study	N/A
MCF10.DCIS.com RAB5A RAC1-2G	This study	N/A
MCF10.DCIS.com RAB5A CDC42-2G	This study	N/A
HEK293T	ICLC	N/A
Oligonucleotides		
siRNA targeting sequence: MYO6 #1: 5′-GAGGCUGCACU AGAUACUUUGCUAA-3′	Thermo Fisher Scientific	NM_004999_stealth_1106
siRNA targeting sequence: MYO6 #2: 5′-GAGCCTTTGCCA TGGTACTTAGGTA-3′	Thermo Fisher Scientific	NM_004999_stealth_4
siRNA targeting sequence: DOCK7 #1: 5′- UUUAAGGUCA UCUUGAUCAUCCUGG-3′	Thermo Fisher Scientific	Cat # HSS131697
siRNA targeting sequence: DOCK7 #2: 5′- AUUAGGGUAA GUAUUUGGUAGGCGG-3′	Thermo Fisher Scientific	Cat # HSS131695
MYO6 isoform detection by PCR For. Sequence: CCGAG CTCATCAGTGATGAGGC	Wollscheid et al.[31]	N/A
MYO6 isoform detection by PCR Rev. Sequence: CCAAGC ATGATACACTTTTAGTCTCC	Wollscheid et al.[31]	N/A
Primer: DOCK7-FL. Forward: GCGGCCCCGAACTAGTGCCACCATGGTGAGCAAGG	This study	N/A

(*Continued on next page*)

Continued

REAGENT or RESOURCE	SOURCE	IDENTIFIER
Primer: DHR2-LobeBC (aa1795-2072) of DOCK7. EcoRI-Forward: AAAGAATTCCGGATGTTTGGCACCTATTTTC	This study	N/A
Primer: DHR2-LobeBC (aa1795-2072) of DOCK7. XhoI-Reverse: AAACTCGAGTTAAGGGATCTTTCTGTTGATC	This study	N/A
Primer: DHR2-LobeAC (aa1597-2072) of DOCK7. EcoRI-Forward: AAAGAATTCGATCTGGTTTTCAATCTCC	This study	N/A
Primer: DHR2-LobeAC (aa1597-2072) of DOCK7. XhoI-Reverse: AAAGAATTCAAGGGTTACCAGACCTCTCC	This study	N/A
Primer: RAC1 (aa1-177). EcoRI-Forward: AAAGAATTCA TGCAGGCCATCAAGTG	This study	N/A
Primer: RAC1 (aa1-177). XhoI-Reverse: AAACTCGAGTT AGAGGACTGCTCG	This study	N/A
Recombinant DNA		
pLenti-RAC1-2G FRET Biosensor	Fritz et al.[37]	Addgene Plasmid #66111
pLenti-Cdc42-2G FRET Biosensor	Martin et al.[40]	Addgene Plasmid #68813
pGEX-GST-CRIB	Innocenti et al.[59]	N/A
Software and algorithms		
ImageJ	Schneider et al.	https://imagej.nih.gov/ij/
Fiji	N/A	https://imagej.net/software/fiji/downloads
PRISM	N/A	https://www.graphpad.com/features
MATLAB software PIVlab	Thielicke et al.[60]	https://www.mathworks.com/
TSVdb	Sun et al.[61]	http://www.tsvdb.com
Biorender	N/A	Biorender.com

RESOURCE AVAILABILITY

Lead contact

Further information and requests for resources and reagents should be directed to and will be fulfilled by the lead contact, Simona Polo (simona.polo@ifom.eu).

Materials availability

All unique reagents generated in this study are available from the lead contact upon request and with a completed Materials Transfer Agreement.

Data and code availability

- This paper analyzed existing, publicly available data. The accession numbers for the datasets are listed in the key resources table (https://portal.gdc.cancer.gov/projects/TCGA-BRCA).
- This paper does not report original code.
- Raw data from main figures are deposited on Mendeley at https://doi.org/10.17632/zsxcs45pt3.1.
- Any additional information required to reanalyze the data reported in this paper is available from the lead contact upon request.

METHOD DETAILS

Constructs and reagents

GTP-CRIB plasmid[59] and GST-myosin VI (human isoform2, NP_001287828.1) constructs were previously described.[31] pLenti-RAC1-2G FRET Biosensor and pLenti-Cdc42-2G FRET Biosensor were obtained from Addgene (#66111 and #68813, respectively). DHR2 domain of DOCK2, DOCK6 and DOCK9 GEF proteins were amplified by PCR (primers listed in the "key resources table") using cDNA from Caco2 cells, cloned into the expression vector pEGFP-C1 and sequence-verified. pEGFP-DOCK7 was amplified by PCR from pCA-FLAG-DOCK7-FL[62] and cloned into the pEGFP-C1 expression vector. pSLIK-EGFP-DOCK7 and pSLIK-RAC1 wild-type (WT) and P29S constructs were generated starting from previous constructs (pCDNA3-RAC1[63] and pEGFP-DOCK7) with Gateway LR Clonase II Enzyme mix (Thermo Fisher Scientific) by subcloning their respective PCR products into a pENTR vector, followed by recombination into the pSLIK-HYGRO empty vector.

All the other truncated constructs were engineered by site-directed mutagenesis or recombinant PCR and sequence-verified. Briefly, the DHR2 domain of DOCK7 (residues 1597–2072) was amplified and cloned into the pET28a, pET43 and pEGFP-C1 expression vectors. RAC1 (residues 1–177) was amplified and cloned into the pGEX-6P-1 expression vector. DHR2-ΔLobeA of DOCK7 (residues 1795–2072) was amplified and cloned into the pGEX-6P-1 and pEGFP-C1 expression vectors.

Cell lines and transfection procedures

The DCIS-RAB5A cell line and derivatives stably expressing GFP-LifeAct or mCherry-H2B were previously described.[17] Cells were grown at 37°C in humidified atmosphere with 5% CO_2 in Dulbecco's Modified Eagle Medium (DMEM): Nutrient Mixture F-12 (DMEM/F12) medium (Invitrogen) supplemented with 5% horse serum, 0.5 mg/mL hydrocortisone, 10 μg/mL insulin, and 20 ng/mL EGF. Phoenix-AMPHO cells (American Type Culture Collection, CRL-3213) were used as the packaging cell line for the generation of retroviral particles and cultured as recommended by the supplier. HEK293T cells were obtained from the BBCF-Biological Bank and Cell factory, INT, Milan, grown in DMEM supplemented with 10% fetal bovine serum and 2 mM L-glutamine and used as the packaging line for lentiviral vectors.

DCIS-RAB5A cells and derivatives were infected with pSLIK-EV (empty vector, CTR), pSLIK-EGFP-DOCK7-FL or pSLIK-RAC1 WT and P29S and selected with hygromycin to obtain stable inducible cell lines. In the case of DCIS-RAB5A expressing pSLIK-EGFP-DOCK7-FL, cells were FACS sorted with Beckman Coulter MoFlo Astrios to obtain a homogeneous population with low expression of GFP-DOCK7 in order to determine its localization. In these cell lines, doxycycline induction promotes the expression of RAB5A and DOCK7 or RAB5A and RAC1 WT/P29S. All cell lines were authenticated by cell fingerprinting and tested for mycoplasma contamination.

FRET-based analysis of RAC1 and CDC42 activation was performed infecting DCIS-RAB5A cells with pLent-RAC1-2G[37] or pLenti-CDC42-2G[40] second generation FRET biosensors, followed by selection with puromycin to obtain stable inducible cell lines.

Transient knock-down of myosin VI or DOCK7 was performed using Stealth siRNA oligonucleotides (listed in the "key resources table") from Thermo Fischer Scientific (Waltham, MA, USA). Cells were transfected twice using RNAiMax (Invitrogen), first in suspension and the following day in adhesion. Based on immunoblot analyses, cells were considered myosin VI or DOCK7-depleted three days after the first transfection. Two siRNA oligonucleotides/gene were used with comparable results.

Expression of myosin VI isoforms in DCIS-RAB5A cells was assessed by RT-PCR. RNA was isolated from cells grown at different confluencies using Maxwell RSC Instrument and Maxwell RSC simplyRNA Cells Kit. Retro-transcription was performed with QuantiTect Reverse Transcription Kit (Qiagen). The cDNA obtained was amplified by PCR using primers flanking the spliced regions (listed in the "key resources table") as previously described.[31]

Antibodies

The following antibodies were used at the indicated dilutions: anti-His (mouse, 1:1000, Cell Signaling), anti-RAC1 (mouse, 1:1000, BD), anti-E-cad (mouse, 1:200, BD-610181), anti-Desmoplakin (rabbit, 1:1000, NW6; kindly provided by Kathleen Green and Lisa Godsel), anti-myosin VI (rabbit, homemade,[31] 1:5000, Eurogentec-1296), anti-GAPDH (mouse, 1:2000, Santa Cruz-32233), anti-DOCK7 (mouse, 1:1000, Santa Cruz-398888), anti-RAB5A (mouse, 1:1000, Santa Cruz-166600), anti-CDC42 (rabbit, 1:1000, Santa Cruz-2462), and anti-GFP (rabbit, 1:5000, Sigma-G1544).

Single cell migration assay

Random single cell migration experiment was performed as previously described.[14] Briefly, DCIS-RAB5A mCherry-H2B cells were transfected twice with siRNA oligos and seeded in sparse cell growth conditions in six-well plates (5×10^4 cells/well) in complete medium. RAB5A expression was induced 16 h before the experiment was initiated by adding fresh complete media supplemented with 2.5 μg/mL doxycycline to the cells. Cell migration was monitored by time-lapse microscopy. At the time of recording, fresh media containing EGF was added to the cells. The assay was performed using an environmental microscope incubator set to 37°C and 5% CO2 perfusion. An Olympus ScanR inverted microscope with 10× objective was used to acquire images every 5 min over a 24-h period. Tracking of cell nuclei and motility analysis were performed as described below.

For confined migration experiment, we employed fibronectin-coated micro-patterned lines of 10 μm diameter created through photolithography.[64] Briefly, glass coverslips were activated with plasma cleaner (Harrick Plasma), followed by coating with PLL-g-PEG (Surface Solutions GmbH, 0.1 mg/mL). After washing with phosphate-buffered saline (PBS), the surface was illuminated with UV light (UVO Cleaner, Jelight) using chromium photo-masks (JD-Photodata). The coverslips were then incubated with fibronectin (25 μg/mL), and 10^4 DCIS-RAB5A mCherry-H2B transfected cells were seeded over-night with 2.5 μg/mL doxycycline prior to analysis. Images were acquired every 5 min for 24 h using a humidity- and temperature-controlled inverted wide-field ScanR microscope. Tracking of cell nuclei and motility analysis were performed as previously described using a developed C++ software with the OpenCV [http://opencv.willowgarage.com/wiki/] and the GSL [http://www.gnu.org/software/gsl/] libraries. The migration analysis was performed by the C++ software coupled with R [www.R-project.org].

Wound healing assays

Assays were performed as previously described.[14] Briefly, cells transfected in suspension were seeded at confluency in six-well plates (1.5×10^6 cells/well) in complete medium and transfected again the following day. Three days after seeding, a uniform

monolayer is formed. RAB5A, DOCK7 and RAC1 WT/P29S expression was induced 16 h before the experiment was initiated by adding fresh complete media supplemented with 2.5 μg/mL doxycycline to the cells. The cell monolayer was scratched with a pipette tip and carefully washed with PBS to remove floating cells and create a cell-free wound area. The closure of the wound was monitored by time-lapse microscopy. At the time of recording, fresh media containing EGF was added to the cells. The assay was performed using an environmental microscope incubator set to 37°C and 5% CO_2 perfusion. An Olympus ScanR inverted microscope with 10× objective was used to acquire images every 5 min over a 24-h period. The percentage of area covered by cells (area coverage %) over time and wound-front speed were calculated using a custom Fiji and MATLAB code. The area covered over time was fitted with a straight line whose slope was used to estimate the velocity of wound closure.

Measurement of the cellular velocities and trajectories

To measure velocity and trajectories of the cells at various distance from the edge of the wound we used Fiji Trackmate plugin [10]. The obtained tracks were separated in three different area: FRONT (<50μm from the wound edge), MIDDLE (50μm < wound edge <150μm) and BACK (150μm < wound edge <300μm) according to the cell distance from the wound edge. The FRONT area corresponds to $n \leq 3$ cells in a row.

The distance between each nuclei centroid (identified by Trackmate analysis) and the wound edge (identified by the previously described wound healing analysis) was calculated using the MATLAB ''bwdist'' function. For each area (FRONT, MIDDLE, BACK) and for each track the directional change rate (https://imagej.net/plugins/trackmate/algorithms#mean-directional-change) was measured by Fiji Trackmate plugin as the average angle difference between two subsequent displacements. Directionality of the cells belonging to the different area are expressed as the inverse of the directional change rate parameter obtained.

Kymograph analysis of cell protrusions at the wound edge

For cell protrusion analysis at the wound edge, the wound healing assay was performed using Culture Inserts (Ibidi) to avoid debrides affecting the quality of the kymograph analysis. Inserts were placed in a 12-well plate and DCIS-RAB5A transfected cells were plated in each chamber (6×10^4 cells/chamber). A cell-free wound area was created by removal of the insert. Cell migration was monitored by a Leica widefield Thunder imager equipped with a Leica sCMOS DFC9000GT, using a Leica HC PL Fluotar 20× objective, NA 0.5. Images were acquired every 30 s for 1 h (100 ms exposure time). Images from 10 positions/condition were recorded every 30 s over a 1-h period. To measure the dynamic of protrusive structures, each visible lamellipodia was analyzed by tracing a single pixel wide line orthogonally to the edge of the wound. The resulting kymograph was obtained and analyzed following the plugin of the ImageJ Kymograph macro (available at https://www.embl.de/eamnet/html/kymograph.html). Briefly, a segmented line was traced following the edges of the lamellipodia in the kymographs, and every protrusion or retraction in the video were averaged to obtain a single value for the plot. Persistence was calculated considering the total amount of frames in which the protrusion is visible until retraction begins.

In order to extract the lamellipodia region area from phase contrast time lapse images acquired as described above, we used a fully convolutional neural network.[36] The network was trained with 65 images of leading-edge cell protrusions at the wound.

Cell sheet streaming and kinetic parameter measurements

DCIS-RAB5A and derivative cell lines were transfected and seeded as described for the wound healing experiment. RAB5A, DOCK7 and RAC1 WT/P29S expression was induced 16 h before the experiment was initiated with 2.5 μg/mL doxycycline. The assay was performed using an environmental microscope incubator set to 37°C and 5% CO2 perfusion. An Olympus ScanR inverted microscope with 10× objective was used to acquire images every 5 min over a 24-h period.

Quantification of monolayer dynamics in the streaming assays was performed using both Particle Imaging Velocimetry (PIV) and Particle Tracking (PT). PIV analysis of phase-contrast image sequences was performed using the MATLAB software PIVlab.[60] In all cases, we adopted a final interrogation area of $20.8x20.8\ \mu m^2$, close to the typical cell projected area. Spurious contributions to the velocity field corresponding to instantaneous global translations between consecutive frames (due to stage positioning errors) were removed through the smoothing procedure described in.[65]

From the resulting velocity field $\boldsymbol{v}(\boldsymbol{x},t)$, where $\boldsymbol{x}$ is the position in the monolayer plane, the root mean squared velocity v_{RMS} and the polar order parameter ψ were computed as:

$$v_{RMS} = < \sqrt{\langle |\boldsymbol{v}|^2 \rangle_{\boldsymbol{x}}} >_{j,t}$$

$$\psi = \left\langle \frac{|\langle \boldsymbol{v} \rangle_{\boldsymbol{x}}|^2}{\langle |\boldsymbol{v}|^2 \rangle_{\boldsymbol{x}}} \right\rangle_{j,t}$$

Where $< \ldots >_{\boldsymbol{x}}$ denotes the space average while $< \ldots >_{j,t}$ denotes the average over different field of views (FOVs) j and over different time points t. For each experiment, at least 5 different FOV were considered, while the time average was made over a time window from 4 to 20 h after time-lapse recording starts. This time window roughly corresponded to the peak of RAB5A-induced motility.[14]

The velocity spatial correlation function was evaluated from the PIV velocity field as

$$C_{vv}(r) = \left\langle \left\langle \frac{\langle \boldsymbol{v}(\boldsymbol{x},t)\cdot\boldsymbol{v}(\boldsymbol{x}+\boldsymbol{r},t)\rangle_{\boldsymbol{x}}}{\left\langle |\boldsymbol{v}(\boldsymbol{x},t)|^2 \right\rangle_{\boldsymbol{x}}} \right\rangle_{\theta} \right\rangle_{j,t}$$

Where $\langle \ldots \rangle_{\theta}$ denotes the azimuthal average over different orientations of the relative position vector $\boldsymbol{r}$ and $r \equiv |\boldsymbol{r}|$. The obtained velocity space correlation was fitted with a stretched exponential function $C_{vv}(r) = \exp\left[- \left(\frac{r}{l}\right)^{\beta} \right]$. An estimate for the correlation length L_{corr} was obtained by calculating the average decay length $L_{corr} \equiv \int_0^{\infty} dr \exp\left[- \left(\frac{r}{l}\right)^{\beta} \right] = \frac{1}{\beta}\Gamma\left(\frac{1}{\beta}\right) l$, where Γ is the gamma function.

In order to quantify the relative motion between neighboring cells, we performed particle tracking on fluorescent nuclei. The particle tracking algorithm is described in detail in.[65] Briefly, we performed for each frame I a seeded watershed transformation of the gradient image ∇I to segment each fluorescent nucleus k and compute its centers of mass $\boldsymbol{x}_k$, assumed to coincide with the geometrical center of mass of its projection on the plane. Single nuclei trajectories were then obtained by linking nuclei positions in subsequent frames using the available MATLAB implementation by D. Blair and E. Dufresne (http://physics.georgetown.edu/matlab) of the Grier Crocker tracking algorithm.[66] From nuclear trajectories, the instantaneous velocity $\boldsymbol{v}_{INS,k}$ was then evaluated as $\boldsymbol{v}_{INS,k}(t) = [\boldsymbol{x}_k(t+\Delta t) - \boldsymbol{x}_k(t)]/\Delta t$, where Δt is the time between two acquired frames. In order to reduce tracking noise, we computed a weighted moving average $\boldsymbol{v}_k(t)$ by convolving the instantaneous velocity with a Gaussian filter of width 10 min.

We calculated the root mean squared relative velocity Δv_{RMS} of two nuclei at distance r as

$$\Delta v_{RMS}(r) = \left\langle \sqrt{\frac{\int_{r-\delta r}^{r+\delta r} \sum_{k,k'} |\boldsymbol{v}_k - \boldsymbol{v}_{k'}|^2 \delta(r' - |\boldsymbol{x}_k - \boldsymbol{x}_{k'}|) dr'}{\int_{r-\delta r}^{r+\delta r} \sum_{k,k'} \delta(r' - |\boldsymbol{x}_k - \boldsymbol{x}_{k'}|) dr'}} \right\rangle_{j,t},$$

where k and k' run over all nuclei within the same FOV and the amplitude of the integration interval $[r - \delta r, r + \delta r]$ corresponds to 1.3 micrometer. To obtain an estimate of the relative motion of adjacent cells, we evaluated by linear interpolation Δv_{RMS} for $r = 14\ \mu m$, corresponding to the average distance between the center of mass of a nucleus and the ones of its first neighbors.

All of the kinetic parameters were evaluated separately for each independent experiment. Each data point in Figures 1E and 1F, in the central panel of Figure G, and in the left panel of Figure 1G corresponds to independent experiments.

Measurements of cryptic lamellipodia dynamics

Assays were performed as previously described.[14] Briefly, DCIS-RAB5A cells stably expressing EGFP-LifeAct were mixed in a 1:10 ratio with unlabeled DCIS-RAB5A cells and transfected and seeded as described for the wound healing experiment. Cell migration was monitored by time-lapse phase-contrast and fluorescence microscopy with an Olympus ScanR inverted microscope using a 20× objective and images were acquired every 90 s over a 6-h period. The quantification of cryptic lamellipodia protrusion velocity was performed using the ADAPT plug-in of Fiji. Cryptic lamellipodia directionality was measured as the angle Φ delimited by the direction of the single lamellipodium and the direction vector of the collective pack locomotion.

$0^{\circ} \leq \Phi \leq 45^{\circ}$ indicates that protrusion and collective migration have the same direction; $\Phi = 180^{\circ}$ indicates that protrusion and collective migration have opposite directions. The assay was repeated five times for each condition and at least 25 cells/condition were counted for each experiment.

Immunofluorescence (IF)

DCIS-RAB5A cells were grown on coverslips and fixed with 4% paraformaldehyde (PFA) for 10 min. Coverslips were incubated in PBS with 2% BSA for 1 h for blocking, followed by incubation with primary antibodies for 1 h at room temperature (RT) (overnight at 4°C in case of confluent cells) and secondary antibodies for 1 h at RT in PBS containing 1% BSA. Incubation with DAPI (Sigma-Aldrich, cat. D9542) for 10 min was performed to stain the nuclei. Coverslips were mounted on glass slides using Mowiol Mounting Medium (Calbiochem) and images were acquired using Leica TCS SP8 laser confocal scanner mounted on a Leica DMI 6000B inverted microscope equipped with HCX PL APO 63×/1.4 NA oil immersion objective.

For Figure 2B, quantification of the mean fluorescence signal of myosin VI across the cells in Z-stacks images was performed manually using Fiji. The assay was repeated four times and 15 cells/experiment were analyzed.

Colocalization analysis was carried out adapting the JaCOP FIJI4,5 plugin[67] and using a custom pipeline able to process multiple folders and multicolor images. Manders' coefficients[68] were calculated considering phalloidin or myosin VI signal as image A and

DOCK7 signal as image B. For myosin VI-DOCK7 colocalization (Figure 5C), the XZ resliced images of the z-stacks images were split into two parts to distinguish the contribution of the basal and the apical regions of the cells.

FRET based RAC1/CDC42 activation assay

DCIS-RAB5A cells stably expressing RAC1-2G[37] or CDC42-2G[40] FRET biosensors were mixed in a 1:10 ratio with unlabeled DCIS-RAB5A cells and transfected and seeded at confluency on coverslips. Three days after seeding, RAB5A expression is induced for 16 h and coverslips were fixed with 4% PFA for 10 min. Images were acquired with GE HealthCare Deltavision OMX system, equipped with 2 PCO Edge 5.5 sCMOS cameras, using a 60 ×1.42 NA Oil immersion objective.

A custom Fiji plugin was developed to calculate single cell FRET signal. Briefly, YPF channel was used to identify single cell edge allowing background removal (https://imagej.net/plugins/rolling-ball-background-subtraction) and Gaussian filter. The single cells were segmented using the ImageJ Li's threshold method (https://imagej.net/plugins/auto-threshold#li). Cell periphery (<1.5 μm from the edge) was used to quantify the FRET intensity signal. The ratio between the FRET channel and the CFP channel was calculated using a python script to obtain the distribution parameters.

Protein expression and purification

Recombinant proteins were expressed in E. coli BL21 (DE3) at 18°C for 16 h after induction with 0.5 mM IPTG at an OD600 of 0.6.

For GST-fusion proteins, cell pellets were resuspended in lysis buffer (50 mM HEPES pH 7.5, 200 mM NaCl, 1 mM EDTA, 0.1% NP40, 5% glycerol, 0.1 mM PMSF, and 1:500 protease inhibitor cocktail (Calbiochem). Sonicated lysates were cleared by centrifugation at 16,000 rpm for 45 min at 4°C. Supernatants were incubated with 1 mL of glutathione Sepharose beads (Cytiva) per liter of bacterial culture for 4 h at 4°C. Beads were washed four times with lysis buffer followed by four washes with high salt buffer (20 mM Tris-HCl pH 8.0, 1 M NaCl, 1 mM EDTA, 1 mM DTT, and 5% glycerol) and finally equilibrated in cleavage buffer (20 mM Tris-HCl pH 8.0, 200 mM NaCl, 1 mM DTT, and 5% glycerol). PreScission protease was added at a 1:50 (w/w) ratio (protease:substrate) and incubated for 16 h at 4°C. Cleaved proteins were concentrated in Amicon Ultra Centrifugal Filters (MW cut-off 10 and 30 kDa, respectively) (Merck Millipore) and loaded onto a Superdex 75 10/300 GL column (Cytiva) equilibrated with 20 mM Tris-HCl pH 8.0, 150 mM NaCl, 5% glycerol, and 1 mM DTT. Fractions containing purified proteins were collected and concentrated.

For HisMBP-fusion DHR2 (DOCK7), cell pellets were lysed in 50 mM Na-Phosphate buffer pH 7.5, 200 mM NaCl, 10 mM imidazole, and 5% glycerol. After sonication and clearance of the lysate by centrifugation, supernatants were incubated with 1 mL Ni-NTA agarose beads (Qiagen) per 1 L of bacterial culture. Beads were washed four times with lysis buffer followed by four washes with high salt/imidazole buffer (20 mM Na-Phosphate buffer pH 7.5, 1 M NaCl, 30 mM imidazole, and 5% glycerol). Proteins were then eluted from beads with buffer containing 20 mM Tris-HCl pH 8.0, 200 mM NaCl, 300 mM imidazole, and 5% glycerol, and dialyzed over night at 4°C in the same buffer without imidazole. Dialyzed proteins were concentrated and purified by SEC as described for the GST-fusion proteins.

Co-immunoprecipitation and pull-down assays

For co-immunoprecipitation (co-IP) analysis, 1 mg of fresh lysates were incubated with specific antibodies for 2 h at 4°C. Cells were lysed in JS buffer (50 mM HEPES, pH 7.5, 150 mM NaCl, 1.5 mM MgCl2, 5 mM EGTA, 10% glycerol, and 1% Triton X-100) supplemented with 20 mM sodium pyrophosphate, pH 7.5, 250 mM sodium fluoride, 2 mM PMSF, 10 mM sodium orthovanadate, and protease inhibitors (Calbiochem), and lysates were cleared by centrifugation.

For pull-down experiments, 500 μg of transfected HEK293T cellular lysates were incubated with 1 μM of GST-fusion proteins immobilized onto GSH beads for 2 h at 4°C in JS buffer. After extensive washes with JS buffer, beads were re-suspended in Laemmli buffer and proteins were analyzed through sodium dodecyl sulphate–polyacrylamide gel electrophoresis (SDS-PAGE, 4–20% TGX precast gel, Bio-Rad). Detection was performed either by staining the gels with Coomassie or by immunoblotting using specific antibodies.

For the evaluation of direct binding, recombinant GST-fusion proteins (MYO6 tail, MyUb-CBD and RAC1, respectively) immobilized onto beads were incubated with purified HisMBP-tagged DHR2 domain of DOCK7 (15 μM final concentration) for 3 h at 4°C in low salt buffer (20 mM Tris-HCl pH 8.0, 50 mM NaCl, 5% glycerol, and 1 mM DTT). Beads were washed four times with the same buffer supplemented with 1% Triton X- and the samples were run on SDS-PAGE. Detection was performed by immunoblotting using anti-His antibody. Ponceau-stained membranes were used to show equal loading.

The GTP-CRIB assay was performed as described in.[63] Briefly, 500 μg of cell lysates from DCIS-RAB5A mock or myosin VI depleted cell monolayers were incubated with purified GST-CRIB (5 μM final concentration) for 1 h at 4°C. Beads were washed five times with lysis buffer and subjected to SDS-Page followed by immunoblotting with anti-RAC1 or CDC42 antibodies. Quantification was performed by normalizing the intensities of the bands to the total amount of RAC1 in the lysates. Data are reported as fold change with respect to RAC1-GTP levels in the corresponding mock sample for each experiment. Five independent experiments were performed.

AlphaFold2-multimer prediction

The computational resources of the High-Performance Computing Biowulf cluster of the NIH (http://hpc.nih.gov) was used to run AlphaFold2-Multimer. The top-ranking structure from 50 predicted structures was selected for visualization and display. Structures were analyzed and figures generated by using PyMol (PyMOL Molecular Graphics System, http://www.pymol.org).

GEF activity assay

Before starting the assay, all recombinant purified proteins were dialyzed in buffer containing 20 mM Tris-HCl pH 7.0, 150 mM NaCl and 10 mM MgCl2.

Recombinant RAC1 (10 μM final concentration) was pre-incubated with GDP (15 μM final concentration) for 30 min on ice in buffer containing 20 mM Tris-HCl pH 7.0, 150 mM NaCl, 10 mM MgCl2, and 0.2 mg/mL BSA. Subsequently, fluorescent boron-dipyrromethene-fluor (BODIPY-FL)-GTP (2.4 mM final concentration) was added to the GDP-loaded RAC1. To detect intrinsic RAC1 activity, buffer was added to the reaction prior to measurement. As positive control we used EDTA (12 mM final concentration). In the testing conditions, recombinant HisMBP-tagged DHR2 DOCK7 domain was added at the indicated final concentration. To evaluate myosin VI activity, recombinant MYO6 tail construct at the indicated concentration was pre-incubated on ice for 30 min with HisMBP-tagged DHR2 DOCK7 and then added to the reaction mixture. Kinetic hydrolysis of BODIPY-FL-GTP was measured at 30°C by monitoring the increase in fluorescence at excitation/emission wavelengths of 485/535 nm in a black 384-well microplate (Corning) using EnVision (PerkinElmer) plate reader. A reaction containing buffer, GDP and BODIPY-FL-GTP at the same final concentration was set up in order to subtract background value. All reactions were performed in technical triplicates. At the end of the measurement, samples were run on SDS-PAGE and analyzed by Coomassie staining. The assay was repeated at least three times/condition.

IHC analysis and quantification

Formalin-fixed and paraffin embedded (FFPE) tissue samples of human breast cancer cases (8 ductal *in situ* carcinoma and 8 invasive ductal carcinoma cases, collected and handled according to the Helsinki Declaration) were selected for the quantitative *in situ* immunophenotypical analyses. Four-micrometers-thick tissue sections were deparaffinized, rehydrated and unmasked using Novocastra Epitope Retrieval Solutions pH6 in thermostatic bath at 98°C for 30 min. Subsequently, the sections were brought to room temperature and washed in PBS. After neutralization of the endogenous peroxidase with 3% H_2O_2 and Fc blocking by 0.4% casein in PBS (Novocastra, Leica Microsystems), the samples were incubated for 90 min at room temperature with anti-myosin VI primary antibody (code #1296, homemade, 1:250). IHC staining was revealed using Novolink Polymer Detection Systems (Novocastra, Leica Microsystems) and Romulin AEC Chromogen kit (BioOptica) as substrate chromogen. Slides were counterstained with Harris hematoxylin (Novocastra, Leica Microsystems) and analyzed under a Zeiss Axioscope A1 microscope. Microphotographs were collected using a Zeiss Axiocam 503 Color digital camera with the Zen 2.0 Software (Zeiss). Quantitative analyses of IHC staining were performed by calculating the average percentage of positive signals in five nonoverlapping fields at medium-power magnification (200X) using the Positive Pixel Count v9 (2+ moderate positivity and 3+ strong positivity) ImageScope software. Average percentage of positive signals (3+ or 2+) was calculated in five nonoverlapping fields of view (200x). This study was approved by the University of Palermo Ethical Review Board (approval number 09/2018).

Expression profile analysis

The transcriptional myosin VI isoforms expression was analyzed by using TSVdb (http://www.tsvdb.com),[61] using RNA-seq data level of The Cancer Genome Atlas (TCGA) breast cancer (BRCA) dataset which includes 981 invasive breast carcinoma samples (and 112 normal breast samples) with complete clinical and pathological information together with PAM50 and SigClust Subtype assignments. Briefly, we downloaded the normalized expression level (RPKM) of short (isoform_uc003pii) and long (isoform_uc003pih) myosin VI isoforms mapped by TSVdb on GRCh37/hg19 genome assembly. RPKM data were +1 trimmed to avoid ''0'' or ''Null'' values before processing these to obtain ratios of expression between short versus long myosin VI isoforms. Statistical analyses and relative plots were done using JMP 17 (SAS) software.

QUANTIFICATION AND STATISTICAL ANALYSIS

Statistical analyses were performed using JMP 17 (SAS) software or PRISM software package. Statistical tests for data analysis included the log-rank test, Student's t test (two-tailed), and two-way ANOVA. Multivariate statistical analysis was performed using a Cox regression model. p values are reported in each figure legends. $p < 0.05$ was considered statistically significant. *$p < 0.05$; **$p < 0.01$; ***$p < 0.001$; ****$p < 0.0001$. ns, not significant.